Title

Miocene C_4 Grassland Expansion as Recorded by the Indus Fan

Journal

Paleoceanography and Paleoclimatology, 35(6)

ISSN

2572-4517

Authors

Feakins, Sarah J
Liddy, Hannah M
Tauxe, Lisa
et al.

Publication Date

2020-06-01

DOI

10.1029/2020pa003856

Peer reviewed

PLEASE COMPLETE THE PUBLICATION FEE CONSENT FORM BELOW
AND
RETURN TO THE PRODUCTION EDITOR WITH YOUR PROOF CORRECTIONS

Please return this completed form and direct any questions to the Wiley Journal Production Editor at PALOprod@wiley.com.

To order OnlineOpen, you must complete the OnlineOpen order form at:
https://authorservices.wiley.com/bauthor/onlineopen_order.asp
Authors who select OnlineOpen will be charged the standard OnlineOpen fee for your journal, but excess publication fees will still apply, if applicable. **If your paper has generated excess publication fees, please complete and return the form below in addition to completing the OnlineOpen order form online (excess fees are billed separately)**. If you would like to choose OnlineOpen and you have not already submitted your order online, please do so now.

YOUR ARTICLE DETAILS

Journal: *Paleoceanography and Paleoclimatology*
Article: Feakins, S. J., Liddy, H. M., Tauxe, L., Galy, V., Feng, X., Tierney, J. E., et al (2020). Miocene C_4 grassland expansion as recorded by the Indus fan. *Paleoceanography and Paleoclimatology*, 35, e2020PA003856. https://doi.org/10.1029/2020PA003856

OnlineOpen: No **Words:** 10,375 **Tables:** 0 **Figures:** 5 **Total Publishing Units:** 26

Journal Base Fee:		$0
Excess Publishing Units:	1@$125	$125
Publication Fee Total:	USD	$125

An invoice will be mailed to the address you have provided once your edited article publishes online in its final format. Please include on this publication fee form any information that must be included on the invoice.

Publication Fees and Length Guidelines:
http://publications.agu.org/author-resource-center/

Frequently Asked Billing Questions:
http://onlinelibrary.wiley.com/journal/10.1002/(ISSN)2169-8996/homepage/billing_faqs.pdf

Purchase Order Instructions:
Wiley must be listed as the contractor on purchase orders to prevent delay in processing invoices and payments.

WILEY

Author Query Form

Journal: Paleoceanography and Paleoclimatology

Article: palo_20862

Dear Author,

During the copyediting of your paper, the following queries arose. Please respond to these by annotating your proofs with the necessary changes/additions.

- If you intend to annotate your proof electronically, please refer to the E-annotation guidelines.
- If you intend to annotate your proof by means of hard-copy mark-up, please use the standard proofing marks. If manually writing corrections on your proof and returning it by fax, do not write too close to the edge of the paper. Please remember that illegible mark-ups may delay publication.

Whether you opt for hard-copy or electronic annotation of your proofs, we recommend that you provide additional clarification of answers to queries by entering your answers on the query sheet, in addition to the text mark-up.

Query No.	Query	Remark
Q1	AUTHOR: Please fill out the Publication Fee Consent Form in these proofs (including complete mailing address) and return to the Production Editor with your proofs.	
Q2	AUTHOR: Please verify that the linked ORCID identifiers are correct for each author.	
Q3	AUTHOR: Please confirm that forenames/given names (blue) and surnames/family names (vermilion) have been identified correctly.	
Q4	AUTHOR: Please note that your references and their citations have been edited according to APA/AGU style, available at https://publications.agu.org/agu-grammar-and-style-guide/.	
Q5	AUTHOR: Please provide publisher location for Reference “Brown, 2008”.	
Q6	AUTHOR: Please provide publisher location for Reference “Feakins, 2020”.	
Q7	AUTHOR: Please provide the chapter/article page numbers.	
Q8	AUTHOR: Please provide the chapter/article page numbers.	

Please confirm that the funding sponsor list below was correctly extracted from your article: that it includes all funders and that the text has been matched to the correct FundRef Registry organization names. If a name was not found in the FundRef registry, it may not be the canonical name form, it may be a program name rather than an organization name, or it may be an organization not yet included in FundRef Registry. If you know of another name form or a parent organization name for a “not found” item on this list below, please share that information.

FundRef Name	**FundRef Organization Name**
National Natural Science Foundation of China	National Natural Science Foundation of China
U.S. National Science Foundation	National Science Foundation

SPi	Journal Code				Article ID					Dispatch: 00.00.00	CE: JPO
	P	A	L	O	2	0	8	6	2	No. of Pages: 18	ME:

Paleoceanography and Paleoclimatology

RESEARCH ARTICLE
10.1029/2020PA003856

Special Section:
The Miocene: The Future of the Past

Miocene C_4 Grassland Expansion as Recorded by the Indus Fan

Sarah J. Feakins[1], Hannah M. Liddy[1], Lisa Tauxe[2], Valier Galy[3], Xiaojuan Feng[4], Jessica E. Tierney[5], Yunfa Miao[6,7], and Sophie Warny[8]

[1]Department of Earth Sciences, University of Southern California, Los Angeles, CA, USA, [2]Scripps Institution of Oceanography, University of California, San Diego, La Jolla, CA, USA, [3]Department of Marine Chemistry and Geochemistry, Woods Hole Oceanographic Institution, Woods Hole, MA, USA, [4]State Key Laboratory of Vegetation and Environmental Change, Institute of Botany, Chinese Academy of Sciences, Beijing, China, [5]Department of Geosciences, University of Arizona, Tucson, AZ, USA, [6]Key Laboratory of Desert and Desertification, Northwest Institute of Eco-Environment and Resources, Chinese Academy of Sciences, Lanzhou, China, [7]CAS Center for Excellence in Tibetan Plateau Earth Sciences and Key Laboratory of Continental Collision and Plateau Uplift, Institute of Tibetan Plateau Research, Chinese Academy of Sciences, Beijing, China, [8]Department of Geology and Geophysics and Museum of Natural Science, Louisiana State University, Baton Rouge, LA, USA

Key Points:
- Multiproxy study of the Indus fan organic matter reveals that terrestrial sources differ between turbidite and hemipelagic facies
- Carbon isotopes, grass pollen, and charcoal indicate that C_4 grasslands expanded between 7.4–7.2 Ma in hemipelagic facies
- Hydrogen isotopes in plant waxes differ between source regions but do not detect monsoon rainfall changes across the C_4 grassland expansion

Supporting Information:
- Supporting Information S1

Correspondence to:
S. J. Feakins,
feakins@usc.edu

Citation:
Feakins, S. J., Liddy, H. M., Tauxe, L., Galy, V., Feng, X., Tierney, J. E., et al (2020). Miocene C_4 grassland expansion as recorded by the Indus fan. *Paleoceanography and Paleoclimatology*, *35*, e2020PA003856. https://doi.org/10.1029/2020PA003856

Received 17 JAN 2020
Accepted 25 MAR 2020

This article is a companion to 2020PA003857.

Abstract In the late Miocene, grasslands spread across the forested floodplains of the Himalayan foreland, but the causes of the ecological transition are still debated. Recent seafloor drilling by the International Ocean Discovery Program (IODP) provides an opportunity to study the transition across a larger region as archived in the Indus submarine fan. We present a multiproxy study of past vegetation change based on analyses of the carbon isotopic composition ($\delta^{13}C$) of bulk organic carbon, plant wax *n*-alkanes and *n*-alkanoic acids, and quantification of lignin phenols, charcoal, and pollen. We analyze the hydrogen isotopic composition (δD) of plant wax to reconstruct precipitation δD. We use the Branched and Isoprenoid Tetraether (BIT) index to diagnose shifts between terrestrial versus marine lipid inputs between turbidite and hemipelagic sediments. We reconstruct ocean temperatures using the TEX_{86} index only where marine lipids dominate. We find evidence for the late Miocene grassland expansion in both facies, confirming this was a regional ecosystem transformation. Turbidites contain dominantly terrestrial matter from the Indus catchment (D-depleted plant wax), delivered via fluvial transport as shown by the presence of lignin. In contrast, hemipelagic sediments lack lignin and bear D-enriched plant wax consistent with wind-blown inputs from the Indian peninsula; these show a 7.4–7.2 Ma expansion of C_4 grasslands on the Indian subcontinent. Within each facies, we find no clear change in δD values across the late Miocene C_4 expansion, implying consistent distillation of rainfall by monsoon dynamics. Yet, a cooling in the Arabian Sea is coincident with the C_4 expansion.

Plain Language Summary This project studied the mud and sand on the seafloor in the Indian Ocean, west of India and south of Pakistan. We drilled a core through the mud and focused on a section corresponding to 5.5 to 10 Ma. Much of the sand came from the Indus River, but when the river sediments went elsewhere, layers of chalky sediments formed from the shells of marine organisms. Those chalks contain the history of longer spans of time. In the sediments, we found molecular fossils from the waxy coating on plant leaves and the woody parts of plants as well as pollen and charcoal; these point to the types of plants that were growing on land whose remains were washed or blown out to sea. We also found molecular fossils of microbes that lived in the oceans, whose structures indicate ocean temperatures—although when soils washed out in large amounts, ocean temperature estimates are not available. The main finding is that grasses replaced forests across much of the Indian subcontinent and Indus catchment, accompanied by more grass fire and cooler ocean temperatures.

1. Introduction

The Siwalik Group in the Himalayan foothills famously documented a one-step late Miocene expansion of C_4 vegetation, beginning at 7.3 Ma and with almost complete C_4 coverage by 6 Ma (Quade et al., 1989; Quade & Cerling, 1995). This >10‰ shift in the carbon isotopic composition ($\delta^{13}C$) of soil carbonates, has now been replicated in outcrops from Pakistan to Nepal in both soil carbonates and plant wax biomarkers

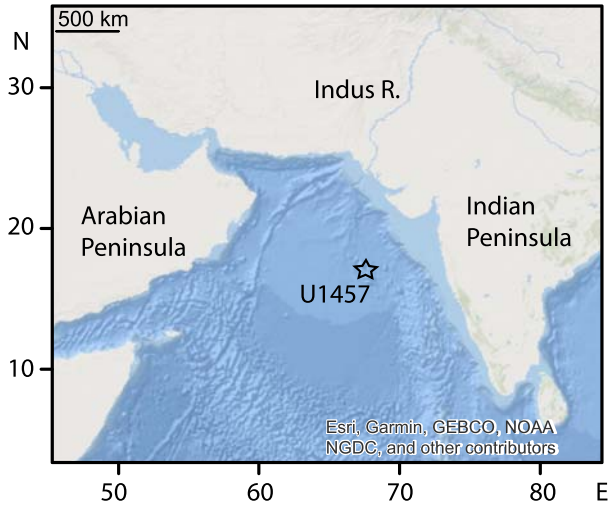

Figure 1. Location of IODP Site U1457.

(Freeman & Colarusso, 2001; Ghosh et al., 2017; Vögeli et al., 2017). Further west, in NE Africa, a 6.5‰ rise in the median $\delta^{13}C$ in fossil teeth enamel of equids reveals a dietary switch, with horses rapidly incorporating C_4 grasses in their diets in the late Miocene (Uno et al., 2011). The timing of the vegetation shift was documented by plant wax records in offshore marine sedimentary archives that indicate a regional expansion of C_4 plants (+4.4‰) soon after 10 Ma (Feakins et al., 2013), later corroborated across N Africa (Polissar et al., 2019; Uno et al., 2016), with reversals and reexpansions of C_4 plants during the Pliocene (Feakins et al., 2005; Levin, 2015; Liddy et al., 2016). Thus, C_4 vegetation expansion around the Indian Ocean does not generally appear as an abrupt, unidirectional transition.

Early studies suggested that the C_4 grassland expansion in Pakistan required a major climatic shift that would have necessarily included the development of a winter dry season and (perhaps) an increase in summer rainfall (Quade et al., 1989). Subsequently, an increase in the relative abundance of the planktic foraminifer *Globigerina bulloides* in the Arabian Sea in the late Miocene was interpreted to indicate an amplification of wind-driven upwelling and thus the summer monsoon (Kroon et al., 1991). Recently, however, that increase in *G. bulloides* has been argued to be an artifact of enhanced carbonate preservation caused by the coincident uplift of the Owen Ridge (Rodriguez et al., 2014) and efforts at replication of *G. bulloides* counts from different locations revealed problematic sensitivity to shell size and bathymetry (Gupta et al., 2015). Furthermore, an increase in cold-tolerant *G. bulloides* could simply reflect a cooling of upwelled waters. This latter interpretation is consistent with evidence for the late Miocene global deep ocean cooling (Holbourn et al., 2013; Holbourn et al., 2018; Lear et al., 2000; Lear et al., 2015). In terms of the surface ocean temperature effects, in the northern Arabian Sea, the late Miocene variability of sea surface temperatures (SSTs) is as yet uncertain, as alkenone $U^{k'}_{37}$ values at Site 722 (Herbert et al., 2016; Huang et al., 2007) hit the upper limit of the paleothermometer and are thus invariant, leaving any change in proximal SSTs associated with the C_4 grassland expansion an open question.

The nature of the C_4 vegetation transition is not well-known south of the Siwalik Group sediments where the grassland expansion was first documented. Expedition 355 of the International Ocean Discovery Program (IODP) provided a first opportunity to sample Miocene sediments eroded mostly from the lowland Indus Catchment. Although the Indus River now barely flows to the ocean with damming and water use for agriculture, in the past, high sediment loads (Milliman & Syvitski, 1992) built the second largest megafan (Métivier et al., 1999).

In this study, we reconstruct vegetation change as recorded by the late Miocene sediments from IODP Site U1457 (Figure 1), collected in 2015 during IODP Expedition 355 to the Indus Fan (Pandey et al., 2015). F1 Late Miocene age sediments comprise voluminous and rapidly emplaced turbidic deposits, and slower accumulation rate hemipelagic sediments. We characterize the provenance of terrestrial vegetation inputs using a combination of inorganic and organic geochemical evidence to differentiate fluvial transport from the Indus River catchment and wind-blown inputs from peninsular India. We seek evidence for vegetation change within each source region based on carbon isotopic composition of bulk organic carbon, plant waxes, and compositional analysis of lignin phenols and pollen assemblages. Drivers of vegetation change that we investigate here include fire (based on measurements of charcoal), hydroclimate (based on hydrogen isotopic analyses of plant waxes), and ocean temperature (based on glycerol dialkyl glycerol tetraethers, GDGTs) in order to provide new insights into the regional nature and drivers of the ecological transition.

2. Materials and Methods

2.1. Marine Sediments and Age Model

IODP Expedition 355 drilled Site U1457 (17°9.95′N, 67°55.81′E, 3,523 m water depth) in the eastern, distal region of the Indus Fan, ~760 km S of the Indus River mouth (Pakistan) and ~490 km west of India (Figure 1). U1457 is located in the western Laxmi Basin, at the foot of the Laxmi Ridge (Pandey

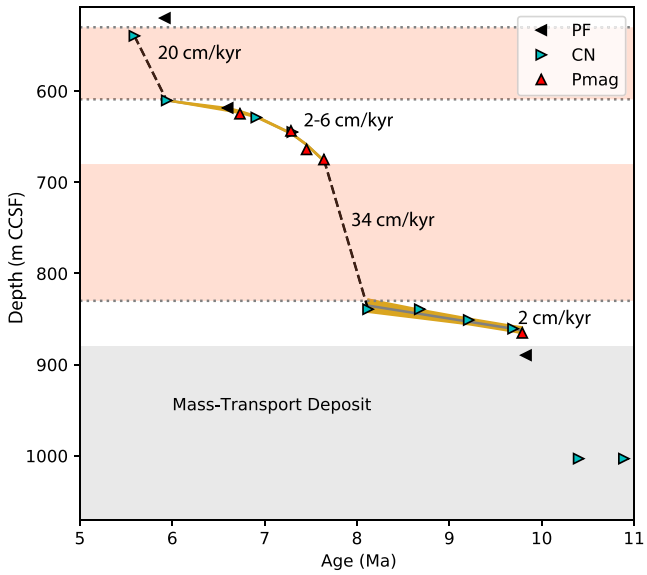

Figure 2. Age model for IODP Site U1457C using age control first and last appearance datums for foraminifera (PF, black triangles) and nannofossils (CN, blue triangles) (Routledge et al., 2019) with refined paleomagnetic chronostratigraphy (Pmag, red triangles) (Tauxe & Feakins, n.d.). Age model and uncertainty (yellow shading) for hemipelagic sediments, with turbidites underconstrained resulting in a linear age model between two points (dashed lines), and erosional unconformities (dotted lines).

et al., 2015). Although the Indus Fan was largely built from N-S erosion along routes similar to the present Indus River (Bourget et al., 2013; Métivier et al., 1999), drilling at U1457 sampled 190 m of a mass transport deposit (MTD), the Nataraja submarine slide. This event is estimated to have moved 19,000 km^3 of sediment from the continental shelf of peninsular India to the Laxmi Basin (Calvès et al., 2015). Although the triggering mechanism is unknown, the event has been tightly dated to between 9.83 and 9.69 Ma (Routledge et al., 2019). The present study begins above the MTD (above 880 m) as the MTD lacks the stratigraphic integrity needed for paleoclimate reconstruction.

The late Miocene accumulations above the MTD are mostly turbidic: silty sands with sharp erosive bases grading upward to clay (Pandey et al., 2015). Recovery is discontinuous (52%) as is common in coarse sediments. Mineralogical analyses indicate that the turbidites, delivered episodically from the shelf, consist mostly of sediments from the southward flowing paleo-Indus River (Pandey et al., 2015). Sediments originating from the Indus River, have been transported through canyons bisecting the continental shelf, delivering turbidity currents into the Indus Fan along channels and building associated levees (Bourget et al., 2013). The locus of deposition has shifted laterally over hundreds of kilometers, and one of these transport channels supplied material to the Laxmi Basin, located in the easternmost region of the fan (Pandey et al., 2015). Such turbidites are known to be efficient mechanisms to deliver (fluvially exported) terrestrial carbon to the deep sea (France-Lanord & Derry, 1997). Additional inputs may derive from westward flowing rivers draining the Indian subcontinent, such as the Narmada and Tapti Rivers (Kessarkar et al., 2003; Yu et al., 2019).

Interspersed between the turbidites is nannofossil ooze, characterized by a mixture of marine carbonates and terrestrial clays. During periods of hemipelagic deposition, eolian influx is likely the dominant conveyor of terrestrial material (Prins et al., 2000). During these periods, Eastern Africa, Arabian Peninsula, Pakistan, and peninsular India could all contribute terrestrial material to the Arabian Sea. However, modern studies of the eastern marginal seas indicate plant wax from the proximal Indian subcontinent, blown in by winter easterlies (Dahl et al., 2005).

The age model for U1457 is based on nannofossil and foraminiferal datums (Routledge et al., 2019) with refined paleomagnetic datums and age model calculation with error estimation (Figure 2) (Tauxe & Feakins, n.d.). Ages are on the Geological Time Scale 2012 (GTS 2012) (Gradstein et al., 2012). Depths in this core refer to the core composite depth below seafloor (CCSF) depth scale in meters throughout. In two mostly hemipelagic sections (880–850 m CCSF and 680–620 m CCSF) sufficient age control exists to constrain an age model and associated uncertainty (Tauxe & Feakins, n.d.). The limitations of dating turbidic sediments is that there are few available age control points and a highly episodic depositional system. In those sediments age estimation is thus limited to linear interpolation between the constraints in the adjacent hemipelagic units.

There are drastic changes in sedimentation rate associated with the mode of sediment delivery: Turbidites have episodic and sometimes voluminous accumulation while hemipelagic sediments have lower and more stable sediment accumulation rates. Between 9.83 and 8 Ma, sediment accumulation rates average ~2 cm kyr^{-1} including hemipelagic sedimentation with age control from the available magnetostratigraphic constraint of the top of Chron C5n at 859 m (9.79 Ma) and from a nannofossil first appearance datum (FAD) at 832 m (8.12 Ma, FAD *Discoaster quinqueramus*). This hemipelagic interval has five age control datums at an average spacing of 0.3 Ma and appears to be well represented by the linear sedimentation rate, although the dating precision can be no better than 0.3 Ma. In this interval consistent sediment accumulation rates provide a sequence suitable for building a paleoenvironmental archive. Above this hemipelagic unit, there is a massive accumulation of turbidites. The erosive base (unconformity) above the 8.12 Ma datum (at 832 m, FAD *Discoaster quinqueramus*) is topped by 158 m of sediment (silty sands), with average

sediment accumulation rates of ~34 cm kyr^{-1}, up to the bounding constraint at 674 m (7.64 Ma, C4n.1r chron). However, there is no available age control within 158 m of turbidites or 0.5 Ma, and accumulation was via episodic delivery of numerous voluminous transport events whose timing cannot be constrained. Between 7.64 and 5.94 Ma, the latter being the nannofossil last appearance datum (LAD) of *Nicklithus amplificus* at 610 m, sediment accumulation rates are 2–6 cm kyr^{-1} including hemipelagic sedimentation above 637 m. This interval has eight age control datums at an average spacing of 0.2 Ma and appears to be well represented by a polynomial fit, with an uncertainty of 0.1–0.5 Ma. It is capped by another accumulation of turbidites, 71 m delivered in 0.4 Ma between the bracketing nannofossil datums (the previous datum and LAD *Discoaster quinqueramus*), although a foraminiferal datum would suggest that it may be even more rapidly emplaced (LAD *Globoquadrina dehiscens*).

We note that uncertainty in the age model comes from both the *y* axis (depth) and the *x* axis (age). Age uncertainty in the hemipelagic units comes from the security of magnetostratigraphic constraints and the age control on the nannofossil datums in the many global records from which they derive. Three of the nannofossil datums have assessed uncertainties of 0.2, 0.1, and 0.01 Ma (Routledge et al., 2019); however, for other microfossil datums the uncertainty has not been quantitatively assessed. Depth uncertainty derives from the resolution of microfossil sampling, from which the LADs and FADs are identified, with sampling only every 9.5 m (core catcher samples) for foraminifera and nannofossils, with an additional survey at 0.75 m for nannofossils after 8 Ma (Routledge et al., 2019). This means the sampling resolution for FADs and LADs was only every ~0.5 Ma in the lower hemipelagic unit, but it was every 0.1 to 0.4 Ma within the younger hemipelagic unit in which the main vegetation transition occurs. The two largely hemipelagic intervals with available age control and relatively consistent sediment accumulation rates, provide the best scope for paleoenvironmental reconstruction, and the C_4 transition on the Indian peninsula is constrained to within 0.1 Ma, by magnetostratigraphy (C3Br.2r) and nannofossil FAD of *Amaurolithus* spp. (Tauxe & Feakins, n.d.).

We examined a total of 52 samples from Site U1457 Hole C, at ~7 m spacing from 500–880 m and ~0.5 m spacing during the interval of slower (hemipelagic) deposition between 600 and 670 m. Within the massive turbidites, graded bedding structures were typically 2–15 cm thick thus each sample corresponds to a distinct turbidite flow from shelf to fan. Samples within hemipelagic sedimentation are 2 cm thick and likely integrate ~1 kyr.

Samples were freeze dried before processing for microfossil counts; and samples for organic analyses were freeze dried then homogenized with a mortar and pestle. Samples were analyzed for a variety of biomarker and geochemical analyses. Epsilon Neodymium (ε_{Nd}) values—that is the $^{143}Nd/^{144}Nd$ offset from the chondritic uniform reservoir, in parts per 10,000—were previously used to study the provenance of Indus Fan detrital material (Clift et al., 2019). Those ε_{Nd} data measured at paired depths with the biomarkers are reported on the new age model here.

2.2. Lignin Phenol Quantification

For CuO oxidation to release lignin-derived phenols, powdered samples were placed in Teflon-lined containers together with 0.5 g CuO, 100 mg ammonium iron (II) sulfate hexahydrate, and 20 mL of 12 M NaOH under N_2, and heated at 170 °C for 2.5 hr. Then, the water phase was acidified to pH < 2 with 6 M HCl and kept for 1 hr at room temperature in the dark to prevent reactions of cinnamic acids. After centrifugation (2,500 rpm for 30 min), the supernatant was liquid-liquid extracted with ethyl acetate. Extracts were rotary evaporated, spiked with an internal quantification standard (ethyl vanillin), and derived with N, O-bis-(trimethylsilyl) trifluoroacetamide and pyridine (70 °C, 1 hr) to yield trimethylsilyl derivatives before quantification by gas chromatograph (GC) mass spectrometry (MS). We quantified lignin phenols using internal standards on a Trace 1310 GC coupled to an ISQ MS (Thermo Fisher Scientific) using a DB-5 ms column (30 m × 0.25 mm, film thickness 0.25 μm). The GC oven temperature was held at 65 °C for 2 min, increased from 65–300 °C at a rate of 6 °C min^{-1}, and held for 20 min. Helium was used as carrier gas (0.8 ml min^{-1}). The MS was operated in electron impact mode at 70 eV and scanned from 50–650 daltons. External quantification standards were used to normalize the response factor for different lignin phenols separately. Vanillyl (vanillin, acetovanillone, vanillic acid), syringyl (syringaldehyde, acetosyringone,

syringic acid), and cinnamyl (*p*-coumaric acid, ferulic acid) phenols were summed to represent lignin phenols (VSC).

2.3. Bulk Organic Carbon Isotopic Analyses

For bulk organic carbon (OC) measurements, powdered samples were weighed into methanol-rinsed Ag capsules and acidified in a vacuum desiccator at 0.5 atm with an open dish with 50 ml 12 N HCl, at 62 °C for 60 to 72 hr (Whiteside et al., 2011), before drying in a vacuum desiccator with indicating silica gel. Samples were packaged in Sn capsules prior to analysis by a Carlo Erba/Fisons 1108 flash elemental analyzer equipped with a Costech ZeroBlank carousel, coupled to a DeltaPlus isotope ratio MS via a Finnigan MAT Conflo II interface for both OC quantification and carbon isotopic analyses ($\delta^{13}C_{OC}$; ‰ Vienna Pee Dee Belemnite, VPDB). A blank and three standards (IAEA-N1 [Ammonium sulfate], USGS-40 [Glutamic Acid], and glycine) were run between every 16 samples and indicate a total OC uncertainty (precision and accuracy) of better than 4%. NBS-19 (limestone) and a calcite laboratory standard were run as unknowns for additional verification of consistency. Carbon isotopic compositions of standards were accurate and precise to better than 0.3‰. N% was measured on nonacidified aliquots and used to calculate OC/N.

2.4. Lipid Extraction and Biomarker Purification

Powdered sediment samples (31.7–95.1 gdw) were extracted with an Accelerated Solvent Extraction system (ASE 350®, Dionex) with 9:1 ratio of dichloromethane (DCM): methanol (MeOH) at 100 °C and 1,500 psi for two 15-min cycles. Extracts were separated over a NH_2 sepra column (5 cm × 40 mm Pasteur pipette, 60 Å) eluted with 2:1 ratio of DCM: isopropanol (neutral fraction) and 4% formic acid in diethyl ether (acid fraction). The acid fraction (containing fatty acids) was methylated with methanol of known isotopic composition with 95:5 MeOH:HCl at 70 °C for 12 hr, before the fatty acid methyl esters (FAMEs) were partitioned into hexane and passed through anhydrous sodium sulfate. Samples were further purified over a silica gel column (5 cm × 40 mm Pasteur pipette, 5% water-deactivated silica gel, 100–200 mesh), washing first with hexane, and then eluting the FAME fraction with DCM. The neutral fraction was loaded onto a silica gel column (5 cm × 40 mm Pasteur pipette, 5% water-deactivated silica gel, 100–200 mesh) and eluted with hexane (*n*-alkanes), DCM, and MeOH (GDGTs). S was removed from the *n*-alkanes by eluting in hexane over activated copper. Further purification included urea adduction when necessary for the *n*-alkanes.

2.5. GDGT Quantification

The fractions containing GDGTs were dissolved in hexane:isopropanol (99:1) and filtered (0.45 μm PTFE) prior to injection on an Agilent 1260 High-Performance Liquid Chromatography (HPLC) coupled to an Agilent 6120 MS. GDGTs were analyzed according to the method of Schouten et al. (2007), using a Grace Cyano column with 5 min isocratic elution using A, and then a gradient of 90% A/10% B to 82% A/18% B over 35 min, where A = hexane and B = hexane:isopropanol (9:1). The column was then backflushed with 100% B for 10 min, and reequilibrated with 90% A/10% B for another 10 min. Single Ion Monitoring mode of the $M + H^+$ ions was used to detect and quantify the isoprenoidal GDGTs produced by marine archaea including GDGTs with 0–3 cyclopentane moieties (GDGT-0 to GDGT-3); crenarchaeol (Cren) with an additional cyclohexane moiety and its regioisomer crenarchaeol′ (Cren′). Following Schouten et al. (2007), TEX_{86} units were calculated using the following equation:

$$TEX_{86} = \frac{[GDGT-2] + [GDGT-3] + [Cren']}{[GDGT-1] + [GDGT-2] + [GDGT-3] + [Cren']}$$

Repeat analysis of a laboratory standard yields a long-term precision of 0.004 TEX_{86} units. We converted the TEX_{86} record to mean annual SSTs using the BAYSPAR calibration (Tierney & Tingley, 2014). For the prior distribution, we used the mean SSTs at the latitude and longitude grid cell (27.6 °C) and a standard deviation of 10 °C (Locarnini et al., 2010). We report total concentrations of branched (brGDGT) and isoprenoidal (isoGDGTs) GDGTs (ng gdw^{-1}) as well as the Branched and Isoprenoidal Tetraether (BIT) index:

$$BIT = \frac{I + II + III}{I + II + III + IV}$$

where I, II, and III represent the abundances of brGDGT and IV represents the abundance of crenarchaeol in each sample (Hopmans et al., 2004). TEX_{86} values in samples with a BIT > 0.4 were considered to be compromised by terrestrial material and thus unreliable for SST estimation.

2.6. Compound Specific Carbon and Hydrogen Isotopic Analyses

The $\delta^{13}C$ and δD isotopic composition of *n*-alkanoic acid and *n*-alkanes were analyzed using a Thermo Scientific Trace GC equipped with a Rxi-5 ms column (30 m × 0.25 mm, film thickness 0.25 μm) with a PTV injector operated in solvent-split mode, coupled to a Delta V Plus isotope ratio mass spectrometer (IRMS) via an Isolink combustion/pyrolysis furnace (1000/1400 °C). Isotopic linearity was monitored daily across a range of peak amplitude (1–8 V) CO_2/H_2 gas pulses. For carbon, the isotopic linearity of $\delta^{13}C$ averaged 0.05‰. For hydrogen, the H_3 factor averaged 4.6 ppm mV^{-1}. Two out of five CO_2/H_2 reference peaks were used for standardization of the isotopic analysis, the remainder track stability. We used external standard runs containing a mixture of 15 *n*-alkanes (C_{16} to C_{30}) with $\delta^{13}C$ values ranging from −33.3‰ to −26.2‰ and δD values ranging from −254.1 to −9.1‰ (A mix; supplied by A. Schimmelmann, Indiana University, USA) to normalize to the VPBD-LSVEC carbon isotopic scale and to the Vienna Standard Mean Ocean Water—Standard Light Antarctic Precipitation hydrogen isotopic scale, respectively. The RMS error of the external standards were better than 4.5‰ for δD and 0.2‰ for $\delta^{13}C$. Samples were run in triplicate, and the average standard deviation was 0.5‰ for carbon and 2.2‰ for hydrogen. The isotopic composition of C added during methylation of *n*-alkanoic acids was determined by offline combustion and dual-inlet IRMS ($\delta^{13}C$ MeOH = −24.7 ± 0.2‰, $n = 6$), and the isotopic composition of H added during methylation was determined by the esterification of phthalic acid for analysis by GC-IRMS (δD MeOH = −187 ± 4‰, $n = 6$). The addition of the methyl group to *n*-alkanoic acids was corrected for by mass balance. The results are reported using delta notation ($\delta^{13}C$ and δD, ‰).

2.7. Palynological Counts: Pollen and Microcharcoal

For palynology, samples were processed using standard chemical palynological processing techniques to extract both pollen and microcharcoal particles. Dry sediment was weighed and spiked with a known quantity of *Lycopodium* spores to allow for evaluation of palynomorph concentrations. Dry sediment was successively treated with hydrochloric acid, hydrofluoric acid, and heavy liquid separation (Brown, 2008). Samples were sieved between a 10 and 250 μm fraction, and the remaining residue was mounted on microscope slides using glycerin jelly. Palynological analysis was conducted on 16 samples in the Louisiana State University's Center for Excellence in Palynology (CENEX) lab. When possible, 300 palynomorphs were tabulated per sample using an Olympus BX41 microscope. Palynomorphs were identified to the lowest taxonomic level possible, and concentrations were calculated as

$$C = (P_c \times L_t \times T)/(L_c \times W)$$

where C = concentration (per gram of dried sediment, gdw^{-1}), P_c = the number of palynomorphs $_{counted}$, L_t = the number of *Lycopodium* spores per tablet, T = the total number of *Lycopodium* tablets added per sample, L_c = the number of *Lycopodium* spores counted, W = the weight of dried sediment. Palynomorph data collection included counts of pollen from terrestrial plants including the Poaceae (grasses) reported as a % of all terrestrial pollen (grass pollen %), as well as ratios (nonaboreal:arboreal; NAP %) and preservation (reworked %).

Microcharcoal was studied in 31 samples. Two basic microcharcoal shapes, long (L) and round (R), were identified from the ratio of length (major axis)/width (minor axis), where $L > 2.5$ and $R < 2.5$, where high L/R ratios indicate more grass fire (Miao et al., 2019). Ratios of big/small charcoal were reported, where big (>50 μm) and small (<50 μm), with larger sizes a semiquantitative indicator of fire proximity, conversely small fragments may be transported further or may experience fragmentation during transport. Total charcoal abundance is normalized to organic carbon concentration, to account for sediment dilution effects, in order to assess proportional inputs of charcoal which may reflect fire frequency and magnitude.

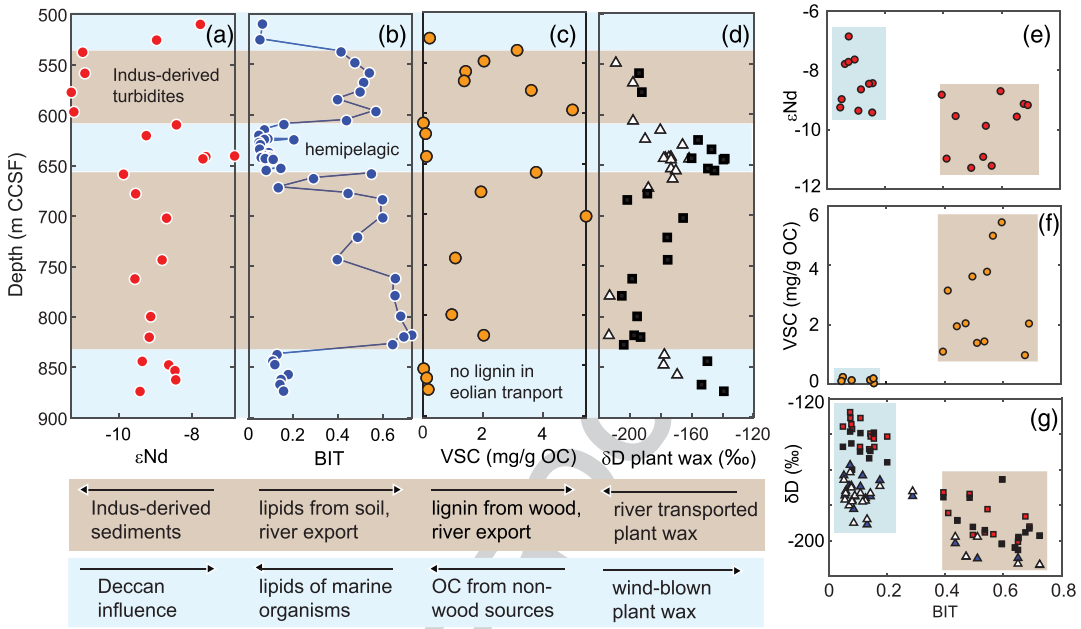

Figure 3. Source characterization based on multiproxy analyses of the same set of samples from Indus fan IODP Site U1457C. Showing depth distribution of (a) ε_{Nd} (Clift et al., 2019) (red circles); (b) the BIT index (blue circle); (c) summed lignin phenols relative to OC concentration (orange circles); and (d) plant wax δD showing example homologs of two compound classes: The C_{31} *n*-alkanes (white triangles) and C_{30} *n*-alkanoic acid (black squares). Bivariate plots showing BIT versus (e) ε_{Nd} (Clift et al., 2019) (red circles), (f) lignin phenols/OC (orange circles), (g) δD of C_{28} *n*-alkanoic acid (red squares), C_{30} *n*-alkanoic acid (black squares), C_{29} *n*-alkanes (gray triangles), and C_{31} *n*-alkanes (white triangles); within compound variation between homologs is less than that between compound class, alkanes are consistently D-depleted relative to alkanoic acids.

3. Results and Discussion

3.1. Stratigraphic Context and Multiproxy Evidence for Provenance of Biomarkers

Although the turbidites dominate volumetrically, remobilized material is mixed and exported in geologically brief interludes. Rapid emplacement of turbidites means that marine influence is minimal and the components are almost entirely terrigenous. In contrast, hemipelagic facies can be sampled with finer temporal resolution despite slower accumulation rates. Although marine productivity dominates, the slow accumulations also archive eolian inputs of terrigenous material. Turbidite and hemipelagic facies are characterized by different inorganic and organic components reflecting their different mode of emplacement and provenance. We find their different characteristics can be described by four proxies in particular: ε_{Nd}, BIT, lignin phenols, and plant wax δD (Figure 3). F3

Nd analyses were previously reported for a subset of the samples analyzed here, and Clift et al. (2019) reported that turbidites in sediments of U1457 of Neogene age (Figure 3a, brown shading) were derived from the Indus River catchment. The Neogene values (ε_{Nd} values of −12 to −9, especially the upper turbidites with ε_{Nd} values of −12 to −11), overlap with the Indus River export during the Holocene (ε_{Nd} − 12 to −10) (Clift et al., 2010), whereas the Pleistocene turbidites are also Indus-derived but more depleted (ε_{Nd} − 14 to −13) (Clift et al., 2019; Yu et al., 2019). Hemipelagic sediments have ε_{Nd} ~ −9.5 to −6.5 and together with other evidence including Sr and clay mineralogy this points to a peninsular India (radiogenic Deccan) source (Clift et al., 2019; Yu et al., 2019) (Figure 3, blue shading), with greater variability consistent with variable sourcing and less mixing in comparison to the turbidites.

The BIT index records clear changes in the proportion of marine versus terrestrial organic inputs with high marine productivity (BIT < 0.2) in hemipelagic sediments and BIT > 0.4 in turbidites indicating a dominance of fluvially transported, soil-derived membrane lipids (Figure 3b). As our focus is the organic component of sediments, we select the BIT proxy with a cutoff of 0.4, to assign sourcing of the biomarkers. Sedimentologic

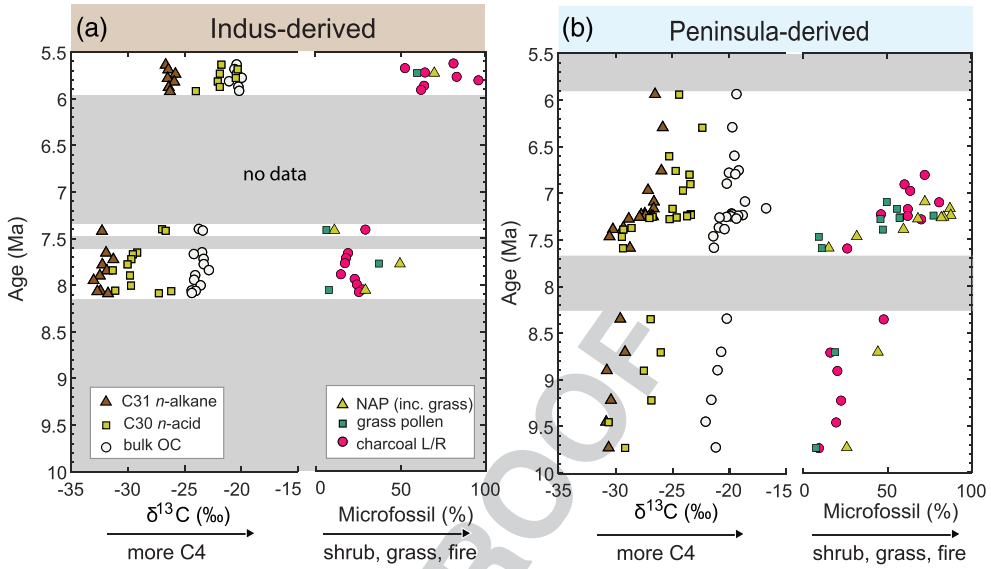

Figure 4. Vegetation indicators from the Indus fan IODP Site U1457C showing (a) fluvially exported material from the Indus River catchment delivered via turbidite currents and recovered from low recovery, but expansive turbidites representing short intervals of time (with bounding age control only); and (b) hemipelagic sediments with an inferred peninsula India source of wind-blown plant proxies (with age control on the C_4 transition being complete by 7.2 Ma to within 0.1 Ma). Within each panel the left-hand axis shows $\delta^{13}C$ plant wax isotope records of *n*-alkane C_{31} (brown triangles) and *n*-alkanoic acid C_{30} (gold squares) as well as bulk organic carbon isotopic values (white circles). The right-hand axis shows microfossil records including nonarboreal (i.e., shrubs and grasses) pollen (gold triangles) and grass pollen (green squares) each as % of all pollen, and long/round charcoal (pink circles) as % of all charcoal (indicates grass-derived charcoal). As the archive represents two delivery mechanisms, separated into panels (a) and (b), the missing time in each archive is indicated (gray shading, i.e., no data).

description of the corresponding core section intervals (based on high-resolution core section images) confirm that this cutoff adequately separates turbiditic and (usually bioturbated) hemipelagic facies.

High lignin phenol content of turbidites confirms fluvial transport of woody plant components. The low lignin phenol content of the hemipelagic layers (Figure 3c) likely indicates negligible fluvial inputs and instead suggests that any terrigenous plant debris (plant wax, pollen, and charcoal) was likely wind blown. Based on Holocene plant wax (Dahl et al., 2005) and Nd evidence for radiogenic, likely Deccan influences (Clift et al., 2019; Yu et al., 2019), we assume a proximal Indian peninsula source for the terrigenous plant debris within Neogene hemipelagic sediments. Studies of Sr-Nd and clay mineralogy have ruled out an Arabian source of dust during the Pleistocene (Yu et al., 2019), as have studies of plant wax provenance in the Holocene, instead finding Indian peninsula sourcing via low-level wind transport in winter easterlies and in the upper troposphere easterlies in summer (Dahl et al., 2005).

Plant wax δD values show abrupt transitions between D-depleted values in the turbidites (−220 to −180‰) and D-enriched values in the hemipelagic sediments (−190 to −130‰, Figure 3d). This is consistent with the BIT evidence for facies changes, the lignin evidence for transport mechanism, and Nd evidence for source switching, between Indus River-derived plant waxes in the turbidites (D-depleted) and those that are wind-blown from India into the hemipelagic units.

3.2. Multiproxy Evidence for C_4 Grassland Expansion

We have generated a multiproxy record of vegetation change based on carbon isotopes and palynomorphs (pollen, microcharcoal), and parsed these using the BIT index to distinguish between facies and thus separate archives of terrestrial vegetation in the Indus catchment (Figure 4a; turbidites) and peninsular India (Figure 4b; hemipelagic), following source characterization described in section 3.1. We report $\delta^{13}C$ values of long chain *n*-alkane (C_{31}) and *n*-alkanoic acid (C_{30}) homologs, both presumed to derive from the waxy coating on plant leaves, as well as for bulk organic matter ($\delta^{13}C_{OC}$) that comprises mostly terrestrial material in turbidites and a mixture of marine and terrestrial production in the hemipelagic facies.

Owing to their high sedimentation rates, turbidites provide only brief glimpses of Indus River catchment conditions at 8.2–7.6 Ma and ~ 7.4 Ma (grouped as 8.2–7.4 Ma), and 5.9–5.6 Ma (Figure 4a), with no internal age control. Nonetheless, the turbidites do allow us to contrast conditions in the Indus catchment before and after the main C_4 grassland transition: all proxies ($\delta^{13}C_{OC}$, $\delta^{13}C_{31alk}$, $\delta^{13}C_{30acid}$, grass pollen, and L/R charcoal) indicate C_4 grass components increased between 7.4 and 5.9 Ma, suggesting an expansion of C_4 grasslands across the Indus River catchment. Comparing the turbidites bracketing the C_4 grassland expansion, we find a shift from −23.8‰ (±0.5‰, $n = 13$) to −20.8‰ (±1.2‰, $n = 9$) in $\delta^{13}C_{OC}$, from −32.1‰ (±0.5‰, $n = 10$) to −26.2‰ (±0.3‰, $n = 7$) in C_{31} *n*-alkanes, from −28.9‰ (±1.7‰, $n = 12$) to −21.7‰ (±1.2‰, $n = 7$) in C_{30} *n*-alkanoic acids. Although a carbon isotopic shift is observed in bulk OC as well as the plant wax components, the relative ^{13}C-enrichment is muted in the bulk, and the absolute values of the OC are ^{13}C-enriched as expected based on the isotopic offset in plants between bulk plants and plant wax and as would be the case if admixed with marine contributions. The OC/N (mean 6.0 ± 1.3, $n = 21$) indicates some marine inputs to the bulk OC emphasizing the need for compound specific approaches to isolate terrestrial organic matter from that of marine inputs. However, the two plant wax compound classes reveal some differences. Before 7.4 Ma the *n*-alkanes (−32.1‰ ± 0.5‰, $n = 10$) suggest a pure C_3 ecosystem, such as woodlands, whereas the *n*-alkanoic acids show more variability (−28.9‰ ± 1.7‰, $n = 12$) that could indicate some C_4 contributions in the 8.2–7.4 Ma turbidites. This offset may reflect differential production of the two compound classes in plants, as there are much greater concentrations of C_{29} and C_{31} *n*-alkanes on the leaves of tropical trees compared to grasses (Garcin et al., 2014), such that C_3 trees may dominate these *n*-alkanes, as also reported in the Mississippi River catchment (Suh et al., 2019). Consistent with this understanding, the C_{33} *n*-alkanes are enriched by up to 1.9‰ (supporting information, Figure S5a), indicating less "dampening" of the grass signal by trees. The C_{30} *n*-alkanoic acid appears to be even more sensitive to the C_4 grassland expansion, with two tentative explanations: leaf production or catchment sourcing. There is little information on relative concentrations of *n*-alkanoic acids produced by grasses, however tropical trees do not produce have a strongly modal distribution of *n*-alkanoic acids as they do with *n*-alkanes (Feakins et al., 2016), such that *n*-alkanoic acids are unlikely to be biased to tree production. Other differences between compound class could arise during fluvial export. Observations from modern catchments that have found that *n*-alkanoic acids tend to have a bias to lowland proximal sources greater than the lowland area would suggest, whereas the *n*-alkanes may retain signatures that are more distally sourced within the catchment arising from inland or higher-elevation erosion (Feakins et al., 2018; Hemingway et al., 2016).

In the Indus River system, we may therefore expect more signs of the upland C_3 forested flanks of the Himalayas in the *n*-alkanes record even after the lowland transitioned to C_4 grassland. Alternatively, isotopic offsets between compound classes could result from nonplant, marine algal or sedimentary microbial input of *n*-alkanoic acids (Kusch et al., 2010; Makou et al., 2018), which could raise the $\delta^{13}C$ values. However why an increase in the microbial contribution would coincide with the vegetation change is unknown and seems unlikely unless this were related to a change in catchment soils and sediment dynamics with the ecological transition. Microfossil evidence confirms the C_4 grassland expansion identified in the bulk organic and plant wax biomarker carbon isotopic evidence. We find that pollen confirms an increase in *Poaceae* (grasses) from 16% (±18%, $n = 3$) to 59% ($n = 1$) and grass-derived charcoal (L/R) from 21% (±55, $n = 8$) to 73% (±155, $n = 8$) between the turbidite sets ending at 7.4 Ma and the next set beginning at 5.9 Ma (Figure 4a) indicates an increase in grass fire. Although it is challenging to convert carbon isotopes to C_4% given the spread in C_3 plants associated with canopy closure resulting in nonunique interpretations, the microfossil evidence supports the *n*-alkanoic acid evidence and allows for roughly a quarter of the lowland biosphere being C_4 grasses or shrubs in the Indus catchment at 7.4 Ma, supporting the interpretation of an early rise of C_4 detected in the *n*-alkanoic acids as a signal of grassland expansion.

In the hemipelagic sediments, we are able to develop a vegetation reconstruction for peninsular India spanning 9.9 to 5.9 Ma. In the earliest part of the record, plant wax carbon isotopic values are close to −30‰ suggesting C_3 ecosystems, and pollen data indicate a mixture of conifers (which grow in montane zones today), Amaranthaceae (subshrubs), grasses, and mangroves suggesting broad sourcing and mixing from mountain to delta. Each of the carbon isotope proxies shows some enrichment around or after 9 Ma. $\delta^{13}C_{OC}$ values show a gradual modest increase after 9 Ma, and the $\delta^{13}C_{30}$ *n*-alkanoic acids show a rise at 8.7 Ma with a single enriched sample (and a large amount of nonarboreal pollen) before a reversal. The main C_4 expansion is

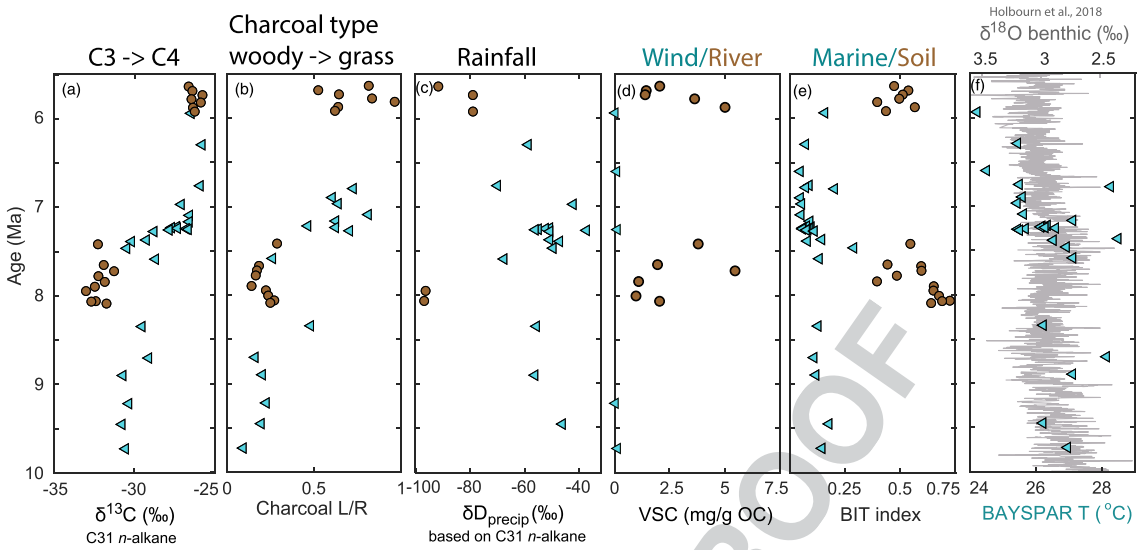

Figure 5. Multiproxy investigation of the possible drivers of C_4 expansion in each region, showing fluvial-turbidite Indus sourcing (brown circles) and hemipelagic sediments with eolian inputs of terrigenous material from peninsular India (blue triangles) to Indus fan IODP Site U1457. (a) $\delta^{13}C$ values of C_{31} *n*-alkanes, (b) microcharcoal long/round (L/R) shape, (c) δD values of paleoprecipitation as reconstructed from C_{31} *n*-alkanes, (d) lignin VSC phenols, (e) BIT index, (f) TEX_{86}-based subsurface temperatures calibrated using BAYSPAR and comparison to $\delta^{18}O_{benthic}$ (gray line) (Holbourn et al., 2018).

complete before 7.2 Ma. $\delta^{13}C_{OC}$ values increase in one main step from −20.9‰ to −18.8‰ between 7.3 and 7.2 Ma. The $\delta^{13}C_{30}$ *n*-alkanoic acid shifts from −29.3‰ at 7.4 Ma to −23.7‰ at 7.2 Ma. The $\delta^{13}C$ of the C_{31} *n*-alkanes increase from −30.2‰ to −26.8‰ from 7.4 to 7.2 Ma indicating an abrupt ^{13}C-enrichment. Correspondence between the carbon isotopic composition of the different proxies reveals their common source in terrestrial vegetation. Subtle differences between the three carbon isotopic archives reflects sensitivity to productivity and degradation pathways that if understood, may reveal useful details. The C_{30} *n*-alkanoic acid record indicates a stronger C_4 expansion than the C_{31} *n*-alkanes in these hemipelagic sediments, as in the turbidites. Evidence from microfossils also informs on the grassland expansion in the hemipelagic sediments. The variability in pollen between samples implies heterogeneity in the wind-exported signal, which may explain divergence in the two compound classes of plant waxes carbon isotope proxies. *Poaceae* (grass) pollen increase from 8% at 7.5 Ma to 47% at 7.4 Ma, and reaching 77% at 7.2 Ma. Thus, pollen is highly complementary to the carbon isotope evidence corroborating the timing of the main C_4 grass rise enveloping the shift in all three archives. Long/round charcoal increases, from <50% before the C_4 transition to >50% after the transition (Figure 4b), reflecting a proportional increase in grasses in combustion (Miao et al., 2019), as would be expected with fire accompanying grassland expansion.

Each of the proxies records the C_4 transition and the subtle differences reveal the challenges of quantitatively establishing the proportion of grassland on the landscape from each of the proxies. As the stronger signals of ^{13}C-enrichment in the *n*-alkanoic acids versus *n*-alkanes are derived from different transport pathways (fluvial vs. eolian) and different source regions (Indus catchment vs. peninsular India) in the two facies, this suggests that the difference in proxy sensitivity originates from the plant wax production in tree leaves swamping the C_{31} *n*-alkane record and underrepresenting the C_4 expansion, compared to the stronger signal of C_4 expansion seen in the C_{30} *n*-alkanoic acids and the microfossil evidence (pollen and grass-derived charcoal).

3.3. Did Fire Drive the C_4 Grassland Expansion?

As C_4 grasslands expanded in both regions (Figure 5a), the increased charcoal abundance (supporting information) suggests that fire promoted savanna grassland expansion and that fire increased as a result of the presence of grasslands (grasslands are more flammable than forests). Other studies have similarly used various measures of fire including charcoal and polycyclic aromatic hydrocarbons to show an increase in fire as

grasslands expand, including during the late Miocene C_4 expansion documented in the Siwaliks (Karp et al., 2018) and in the Pliocene in West Africa (Hoetzel et al., 2013). Here we use the shape of charcoal (Miao et al., 2019), to identify the proportion of grass-derived charcoal (increased L/R, Figure 5b). The increased prevalence of grass fires provides evidence of the feedback role of fire in maintaining grasslands (Beckage & Ellingwood, 2008), as has been shown in modern climates with bistable ecosystems in Africa and South America (Dantas et al., 2016; Staver et al., 2011). Here too in the Indus catchment and peninsula India, it appears likely that fires maintained savanna grassland ecosystems once they appeared, as the transition appears abrupt and unidirectional in the late Miocene, yet in the modern ecosystems C_4 grasses are not dominant, suggesting bistability, at least between forest-grassland in peninsular India (Das et al., 2015), whereas lowland Indus is too dry for grasslands, instead supporting xeric taxa in the late Holocene (Ivory & Lezine, 2009). Modern studies indicate that it is the low dry season precipitation amount that is particularly critical in allowing fire to spread (Das et al., 2015) with the ignition source being lightning that itself exhibits threshold behavior and is climate dependent (Beckage & Ellingwood, 2008). The fire feedback effect may have been enhanced in the Miocene if oxygen levels were elevated through carbon burial as has been hypothesized (Derry & France-Lanord, 1996), helping to maintain C_4 grasslands after they appeared, although no such oxygen evidence is available. An alternate disturbance mechanism comes from cyclonic activity, which can uproot large trees and promote grassland replacement (Beckage & Ellingwood, 2008), with some evidence that Arabian Sea cyclonic activity is increasing associated with anthropogenic warming (Murakami et al., 2017), perhaps also during Miocene warmth.

3.4. Did a Change in Monsoon Rainfall Drive the C_4 Grassland Expansion?

In this study, we sought to test the long-standing question as to whether a change in monsoon precipitation drove the C_4 expansion, using the hydrogen isotopic composition as recorded by plant wax biomarkers as a proxy for precipitation. Within the turbidites, the δD values of C_{31} *n*-alkanes vary between −213‰ and −198‰ (mean − 206 ± 8‰, n = 5, s.e.m. 4‰) and for the C_{30} *n*-alkanoic acids between −205‰ and −166‰ (mean − 191 ± 12‰, n = 13, s.e.m. 4‰). Within the hemipelagic sediments, the δD values of C_{31} *n*-alkanes varies between −190‰ and −162‰ (mean − 175 ± 9‰, n = 16, s.e.m. 2‰) and for the C_{30} *n*-alkanoic acids between −160‰ and −139‰ (mean − 148 ± 7‰, n = 8, s.e.m. 2‰). Thus, the plant waxes in the turbidites are distinctly more D-depleted than the hemipelagic sediments, with no overlapping range. This strongly suggests the different plant wax sourcing of these facies determines their isotopic composition.

In order to calculate estimates of precipitation δD we select a fractionation for tropical forests (Feakins et al., 2016), which is close to the global average value (Sachse et al., 2012) but carries the benefit of calibration of both compound classes used here and surveyed in a large data set. Using an $\varepsilon_{alkane/precip}$ of −129‰ and $\varepsilon_{acid/precip}$ of −121‰ (Feakins et al., 2016) for tropical trees, the central estimates for δD_{precip} are −90‰ based on *n*-alkanes and −80‰ based on *n*-alkanoic acids for sources in the Indus catchment (Figure 5c). The compound class offset fits with the hypothesis that *n*-alkanes may integrate more of the catchment and that *n*-alkanoic acids may be dominantly lowland derived (Hemingway et al., 2016). Uncertainties in the appropriate fractionation (which have not been determined for this region's vegetation), are likely on the order of >10‰. Reconstructed values for the Indus River turbidites are much more D-depleted than modern coastal precipitation sampled by the Global Network of Isotopes in Precipitation (GNIP), in Karachi, Pakistan (IAEA/WMO, 2019) and likely much of the lowland catchment. Indus River turbidites are also more D-depleted than the summer season precipitation in the NE Indus catchment at the GNIP station in Jammu, Kashmir. Although D-depleted precipitation may occur with either winter or summer rainfall maxima during individual storms, observational data indicate that monthly D-depletion is greatest for the highly distilled westerlies and cold-season precipitation (JF monthly mean values < −60‰ at Kabul, Afghanistan) influencing the NW Indus catchment. Summer rainfall in the lowlands is less well constrained by GNIP data, but would likely be between −50‰ (signaling deep convection) and +50‰ (evaporation during descent) based on examination of monthly values for Karachi and very limited data available for Mumbai (IAEA/WMO, 2019). The turbidites instead contain plant wax signals much more consistent with modern winter-dominated precipitation in locations similar to Kabul, Afghanistan (see supporting information for modern climate maps and precipitation isotope data).

Although we are not aware of any modern or Holocene estimates of plant wax δD values transported by the Indus River or exported from the Indus catchment, comparison to processes in the Ganges-Brahmaputra

system (Galy et al., 2011) and other tropical rivers (Feakins et al., 2018; Hemingway et al., 2016) demonstrated export of a minor upland (distal) component mixed with a dominantly lowland (proximal) signature, and thus a lowland (proximal) bias in the exported signal. Yet, the observed Indus River turbidite δD values are D-depleted compared to expected precipitation in the lowland reaches. Thus, it is possible that these late Miocene Indus River exported signatures of plant wax δD in the turbidite facies are more depleted than we would expect for the modern situation, perhaps implying more winter season precipitation (like Kabul, Afghanistan) within a greater portion of the catchment. Alternatively, it is plausible that the Indus catchment may see a greater proportion of upland signal exported from forested regions, given the catchment has a much drier lowland than the Ganges, Congo, or Amazon, with reduced productivity in the lowland grasslands and shrublands. The hypothesis that the Indus River may export the upland biomarker signal to the sea could be tested with future work in modern river or Holocene delta sediments in the Indus River system or in other large montane river networks with dry lowlands.

Given the vegetation transition it may be appropriate to consider selection of a smaller fractionation to represent arid C_3 ecosystems (Feakins et al., 2014; Feakins & Sessions, 2010) and a larger fractionation to represent C_4 grasslands (Smith & Freeman, 2006); however, as there are no locally available calibrations we opt for a fixed fractionation for our reconstructions. We note that if a smaller epsilon were appropriate (as for dryland trees perhaps relevant to the Holocene Indus) then this would make the precipitation more D-depleted (by up to 30‰) (Feakins & Sessions, 2010), pointing further to winter precipitation or upland sourcing in that case. A larger fractionation for grasses after the C_4 expansion would increase the offset in precipitation reconstructed between the two turbidites (Figure 5c), and could imply a drying, or more lowland source. However, any such drying would imply the tree component would shift from moist to dry forest values and the overall plant community average may have very little overall change in fractionation, thus we do not apply a correction given the uncertainties. We further emphasize that all interpretations must remain cautious due to very limited δD data for the turbidites.

Within the hemipelagic sediments, applying the tropical tree fractionation implies a δD_{precip} of −78‰ to −47‰ based on *n*-alkanes or −44‰ to −20‰ based on *n*-alkanoic acids for sources in peninsular India (Figure 5c), which overlaps with the modern range of precipitation isotopes during the Indian Summer Monsoon (supporting information) and indicates similar to modern or perhaps wetter conditions during the late Miocene, with similar circulation and distillation patterns over the Indian peninsula, consistent with evidence for topographic steering and orographic rainout patterns being in place by this time (Acosta & Huber, 2020). The wet tropical forest fractionation appears appropriate for the Western Ghats today and would likewise be appropriate before the C_4 transition. Once again, we do not apply a vegetation correction for possible hydrogen isotope fractionation changes after C_4 expansion, as the difference between tropical C_3 trees and tropical C_4 grasses is not large. Using the slightly larger $\varepsilon_{alkane/precip}$ fractionation for C_4 grasses of −134‰ (Sachse et al., 2012) would adjust the data points after the C_4 transition by +15‰, within the spread of data, and thus would not alter interpretations for the lack of detectable hydroclimate change in peninsular India.

Although we find a large hydrogen isotopic range in U1457 (Figure 5c), this is largely controlled by the change in provenance between facies. The fluvially exported plant waxes in the turbidites (accompanied by river transported lignin, Figure 5d; and soil-derived lipids, with a high BIT, Figure 5e) carry an isotopic composition that is considerably more D-depleted than the wind-blown plant waxes from peninsular India in the hemipelagic sediments (characterized by almost no lignin, Figure 5d; and marine-dominated lipids, with a low BIT, Figure 5e). Although our δD data are sparse, we find no systematic shift in δD within each facies within the available data. Importantly, we find negligible change in the hydrogen isotopic composition of plant waxes in either archive before and after the C_4 transition at 7.2 Ma in peninsular India and between bracketing archives at 7.4 and 5.9 Ma for the Indus catchment.

This lack of plant wax δD shift associated with a plant wax $\delta^{13}C$ shift is also seen in records from West Africa at ~10 Ma (Polissar et al., 2019); however, revisiting their data from DSDP Sites 235 and 241, offshore Somali, do in fact show a 20‰ δD shift associated with the C_4 expansion. Their data are therefore similar to a prior report of a ~10 Ma C_4 expansion (Feakins et al., 2013), accompanied by a 40‰ δD shift, which was interpreted as a drying (Feakins, 2013), from DSDP Site 231 in the Gulf of Aden. Thus, the absence of a hydrogen isotope shift at the C_4 transition in U1457 is similar to reports from West Africa but differs from the pattern

observed in NE Africa. This may denote variations in the degree to which hydroclimate change accompanies the C_4 transition in different regions (Higgins & Scheiter, 2012). Yet, each of these studies (Feakins, 2013; Polissar et al., 2019; and this study), has been conducted at very low resolutions (as low as every ~1 Ma), and future work could usefully seek to probe Miocene hydroclimate variability with higher-resolution plant wax δD studies. And, as the sensitivity of precipitation isotopes to detect hydroclimate transitions varies between climate regimes and regions, the question merits testing with additional proxies for hydroclimate.

3.5. Did Late Miocene Cooling Drive the C_4 Grassland Expansion?

Another driver of the ecological transition has been proposed: related to a global cooling in the late Miocene (Herbert et al., 2016). Here we generate new data for ocean temperatures to test this hypothesis. The turbidite facies have high BIT values (>0.4) which indicates that soil inputs of GDGTs dominate, compromising the TEX_{86} thermometer (Figure 5e). In the hemipelagic sediments, however, the BIT values were low (mostly <0.2) indicating mainly a marine source of GDGTs, thus TEX_{86}-based temperature estimates were converted using the BAYSPAR calibration (Figure 5f). Ocean temperature estimates have central values of 28 to 24 °C. The absolute values of the reconstructed ocean temperatures have uncertainties that are rigorously quantified and that are on the order of ~4 °C. Previous work in the Arabian sea and Gulf of Aden suggests that TEX_{86} may represent subsurface waters (Liddy et al., 2016; Tierney et al., 2016). Given these uncertainties more emphasis should be placed on the trends in the temperature data and we see a cooling of 4 °C across 10–5.5 Ma, with a 1 °C step shift close to 7.3 Ma (Figure 5f). This differs from a nearby alkenone record which remained at the upper limit of that paleothermometer at nearby ODP Site 722 throughout this span (Huang et al., 2007). Although the absolute temperatures may be underestimates, the cooling trend is likely robust and detects a late Miocene cooling of surface waters, such as via increased upwelling in the Oman margin or cooling of the deep ocean and thus cooling of the upwelled water mass. The finding of a late Miocene cooling trend here is furthermore consistent with reports of a global late Miocene cooling in an analysis of available alkenone-based SST estimates (Herbert et al., 2016), and in foraminiferal Mg/Ca paleothermometers (Holbourn et al., 2018). It is also consistent with the evidence for deep ocean cooling (Holbourn et al., 2013; Lear et al., 2000), as well as reports of cooling in upwelling zones in the Arabian Sea (whether due to upwelling intensification or cooler upwelled waters) based on the abundance of cold-loving *Globigerina bulloides* foraminifera (Gupta et al., 2015; Kroon, 1988). Changes in SSTs and in particular SST gradients are found likely to affect monsoon rainfall in idealized (Lutsko et al., 2019) and high-resolution climate model experiments (Acosta & Huber, 2020).

We present the TEX_{86}-based BAYSPAR temperature reconstructions in the context of an orbitally resolved foraminiferal record from the South China Sea where benthic $\delta^{18}O$ record high-latitude temperatures and Antarctic ice volume instability with obliquity pacing (Holbourn et al., 2018) (Figure 5f). Both estimates are on the GTS 12 time scale and well dated, thus we can compare the discrete TEX_{86}-based estimates with the orbitally resolved record, finding good agreement. For example, the warmest TEX_{86} estimate of 28.5 °C at 7.37 Ma corresponds to a warm and low ice volume "interglacial" (one of the lightest benthic $\delta^{18}O$ values). Independent corroboration of locally warm temperatures in that same sample at 7.37 Ma comes from the palynomorph analysis that includes dinoflagellates and a species, *Operculodinium israelianum,* that is normally found in waters with summer maxima >29.2 °C (Marret & Zonneveld, 2003), together providing compelling evidence that Indian Ocean SSTs warmed in phase with the high latitudes. At the other extreme, we find several consecutive cooler estimates near 7.2 Ma (Figure 5c), which correspond to a "prolonged cold event" (Holbourn et al., 2018) where the obliquity-paced cycles appear to "skip a beat" at an eccentricity low.

Basic C_4 energetic theory predicts that the combination of low pCO_2 and warmer temperatures promote C_4 competitive advantage (Ehleringer et al., 1997); however, additional factors influence competition and the interplay of factors is complex. Mean annual precipitation and its seasonal distribution is a key factor in tree cover versus grassland (Cotton et al., 2016; Guan et al., 2014). pCO_2 thresholds vary with rainfall amount, with C_4 found in drier climates at lower pCO_2 (Higgins & Scheiter, 2012), and conversely in the higher than preindustrial pCO_2 levels of the Miocene, C_4 tropical grasslands may have been found in rainfall regimes that today support forests. In tropical mountains of western peninsular India, cool season temperatures are found to limit tropical trees, but warm summers allow C_4 grassland patches at ~2,000 m above sea level today and the ecosystems are thought to be bistable (Das et al., 2015). In bistable ecosystems, where either forest or grassland could exist, other factors of recruitment and disturbance may control the

forest-grassland transition including fire (Beckage & Ellingwood, 2008; Higgins & Scheiter, 2012). Transitions are expected to be abrupt and with a hysteresis effect, for example, as grasses are more flammable than trees so the threshold fire frequency to maintain grasses is lower than that needed to clear forest (Beckage & Ellingwood, 2008).

During the last Pleistocene glacial, abundant C_4 grasslands have been reported from the lowlands of the Ganges-Brahmaputra catchment (during Heinrich Stadial 1) interpreted as a response to lowered pCO_2 and drying, followed by C_3 replacement and mixed ecosystems in the Holocene as monsoon rainfall increased (Agrawal et al., 2014; Contreras-Rosales et al., 2014; Hein et al., 2017). Similarly, C_4 grasslands expanded in the Western Ghats where forests were increasingly limited by cooler temperatures and reduced summer rainfall (Caner et al., 2007). In contrast dry conditions in the (already dry) glacial in the Indus catchment did not promote grasses and instead grasses expanded in the wetter early Holocene (Ansari & Vink, 2007). Thus, the triggers for C_4 expansion vary within the region with varied different tipping points for grassland conditions according to the local context.

Whether the late Miocene C_4 expansion was driven by similar-to-glacial-transition drivers—a drop in pCO_2, cooling and drying—remains an open question. Evidence for a late Miocene pCO_2 drop has long been elusive since first proposed (Cerling et al., 1997). It was initially rejected by alkenone based estimates (Pagani et al., 1999) but more recently found some support from diatom associated organics, calcification, and boron isotopes, although the data remain very preliminary (Badger et al., 2013; Bolton et al., 2016; Mejía et al., 2017; Sosdian et al., 2018). New solutions may emerge, for example, refinements to the alkenone method (Zhang et al., 2019) and there is a keen interest in detailed, robust pCO_2 reconstructions in order to understand the drivers of this late Miocene ecological transformation. During the prolonged cold event near 7.2 Ma, Holbourn et al. (2018) infer a drop in pCO_2 based on a greater difference between the $\delta^{13}C$ of planktic and benthic foraminera. However, alternative possibilities could explain the increased offset, including habitat changes in foraminiferal communities, changes in ocean ventilation influencing the benthic values (Keigwin, 1979) and enrichment of the carbon isotopic composition of the terrestrial biosphere altering that of the atmosphere and surface ocean—that is, the C_4 expansion could lead to a ^{13}C-depletion in the residual pool in the atmosphere and planktic carbonates (Derry & France-Lanord, 1996). While, the C_4 expansion is time-transient around the tropics, the grassland expansion described here, at first gradual and then abruptly switching at 7.2 Ma described here, seems to coincide with gradual and then abrupt change at 7.2 Ma with the final phase of the oceanic carbon isotope shift complete by 7.0 Ma (Holbourn et al., 2018). This correspondence allows for the possibility that the terrestrial vegetation drives the abrupt change in the ocean isotopic balance.

At this time, detailed and multiproxy confirmatory evidence of the carbon dioxide record for the late Miocene—and any possible ties to C_4 expansion—remains elusive, including in recent climate model experiments for North America with a responsive biosphere (Lee, 2019). As independent evolutionary C_4 innovations occurred across the tropics, we should anticipate that the ecological response of the local species may differ and would be triggered by the specific interplay of climatic factors that trigger local ecologic tipping points. The likely answer then to what caused the C_4 expansion appears to be multifactorial regional drivers and regional ecological response (Osborne, 2008). The timing of the response to even a global forcing such as declining carbon dioxide levels would be expected to yield time-transitions based on regional tipping points (Higgins & Scheiter, 2012).

4. Conclusions

In this study of late Miocene sediments of Indus Fan at IODP Site U1457, we find distinct changes in sedimentation rate and composition between turbidites and hemipelagic sediments. We present a multiproxy biomarker and microfossil study of the terrigenous components in these sediments and determine that provenance switches between facies, implying two discontinuous archives within one core. Our primary marker for the facies-based interpretation is the lipid index, the BIT ratio indicating the dominance of soil microbial inputs (BIT > 0.4 in turbidites) or marine microbial inputs (BIT < 0.2 in hemipelagics). Supporting evidence comes from lignin phenols, which establish transport method (fluvial vs. eolian), with only fluvial transport delivering lignin to turbidites but not to the hemipelagic facies. Plant wax δD provides confirmatory evidence

of source switching with more D-depletion in the plant wax from the Indus derived turbidites, compared to D-enrichment in wind-blown waxes from the Indian peninsula.

We observe a vegetation change in each source region within our facies-specific reconstructions. In the turbidites we have massive accumulations but only brief windows of time represented. The available turbidites can only bracket the C_4 expansion in the Indus River catchment to between 7.4 and 5.9 Ma. We find the hemipelagic sediments allow for a detailed investigation of the nature of the transition on peninsular India. Although there is likely some C_4 present by 8.7 Ma, the main transition is revealed in bulk OC, plant wax *n*-alkanes and *n*-alkanoic acids to occur across 7.4 to 7.2 Ma (dated to within 0.1 Ma), with supporting data from grass pollen and grass-derived charcoal.

We see a marked increase in charcoal abundance suggesting more fire on the landscape cleared forests and that grass fire (elongate charcoal) increased proportionally as grasslands expanded. The flammability of grasses, known to be a key feedback mechanism in maintaining grasslands in bistable ecosystem conditions, allowed for the persistence of C_4 grasslands once they appeared in both regions and explains the step shift in vegetation observed on peninsular India.

Paired analysis of plant wax δD and $\delta^{13}C$ does not diagnose whether the monsoon precipitation changes drove the C_4 expansion in the region, as the δD value of plant waxes and thus the reconstructed isotopes of precipitation are found to be dominated by source changes in this archive. Within facies we are unable to identify a clear change in precipitation isotopic composition associated with the C_4 expansion. The sparse data suggest that the hydroclimate of the Indian peninsula was broadly similar to today, at least as detected by precipitation isotopes, although the Indus River catchment may have been more strongly influenced by westerly winter precipitation (more D-depleted) than today. A change in monsoon rainfall may not be the culprit for C_4 expansion or possible grasslands could respond to a precipitation change that was not detected by these plant wax precipitation isotopic proxies, such as a reduction of dry season precipitation that would also promote the observed increase in fire. While we have no evidence for drying here other than the increase of grasslands and fire, bistable ecosystems that display hysteresis behavior may not require much of a climatic shift to trigger a transition of the kind observed in the late Miocene.

Lowering of atmospheric pCO_2 may have both cooled the global climate and also directly increased the competitiveness of C_4 grasses—pCO_2 reconstructions allow this but remain tentative for the late Miocene. A late Miocene cooling has been identified elsewhere, and our TEX_{86} data shows this cooling was reproduced locally in the Arabian Sea. Arabian Sea cooling was likely in part driven by cooling of the high latitudes and thus deep waters affecting the temperature of upwelled waters and in part by radiative changes associated with a drop in pCO_2. Although our low-resolution record aliases some of the orbital variability seen elsewhere, we have finely resolved sampling that shows a cooling of >1 °C at 7.3 Ma (dated to within 0.1 Ma) and overall variability and cooling on the order of 4 °C. It is therefore possible that the cooling of the Arabian Sea was implicated in the ecological transition, perhaps by drying the dry season, which would be the most likely explanation for the increase in fire observed here. However, the ocean-atmosphere connection that hypothetically linked cooler with reduced rainfall, remains elusive because of the lack of a rainfall shift detected by hydrogen isotopes in plant waxes here. It is possible that only modest climatic changes are needed to trigger and maintain ecological switches in bistable ecosystem settings once the C_4 innovation appeared.

Author Contribution Statement

S. F. designed and led the study. H. L and L. T. were shipboard scientists. The following contributed analyses and interpretations: H. L and S. F. (plant wax); L. T. (age model); V. G. (bulk organics); J. T. (membrane lipids); X. F., (lignin); Y. M. (charcoal), and S. W. (pollen). S. F. analyzed and interpreted the multiproxy data, graphed the results, and wrote the manuscript. All authors contributed to the study.

Acknowledgments
We declare no financial conflicts of interests for any author or their affiliations. This research was funded by the U.S. National Science Foundation (OCE 14-50528 to Consortium for Ocean Leadership, subaward GG0093093-01 to S. Feakins, subaward GG0093093-01 to S. Warny, subawards GG0093093-01 and EAR 1547263 to L. Tauxe); microcharcoal analyses were supported by the National Natural Science Foundation of China Grant 41772181. This research used samples and/or data collected by the International Ocean Discovery Program, supported by funding from the U.S. National Science Foundation and other member nations. We thank all participants of the shipboard science party and crew on Expedition 355. We thank the following for laboratory assistance: A. Figueroa, J. Sunwoo, and C. Johnson. Data files are archived at the NOAA paleoclimatology database at https://www.ncdc.noaa.gov/paleo/study/28792 (Feakins, 2020).

References

Acosta, R. P., & Huber, M. (2020). Competing topographic mechanisms for the summer Indo-Asian monsoon. *Geophysical Research Letters*, *47*(3). https://doi.org/10.1029/2019gl085112

Agrawal, S., Galy, V., Sanyal, P., & Eglinton, T. (2014). C4 plant expansion in the Ganga Plain during the last glacial cycle: Insights from isotopic composition of vascular plant biomarkers. *Organic Geochemistry*, *67*, 58–71. https://doi.org/10.1016/j.orggeochem.2013.12.007

Ansari, M. H., & Vink, A. (2007). Vegetation history and palaeoclimate of the past 30 kyr in Pakistan as inferred from the palynology of continental margin sediments off the Indus Delta. *Review of Palaeobotany and Palynology*, *145*, 201–216. https://doi.org/10.1016/j.revpalbo.2006.10.005

Badger, M. P. S., Lear, C. H., Pancost, R. D., Foster, G. L., Bailey, T. R., Leng, M. J., & Abels, H. A. (2013). CO_2 drawdown following the middle Miocene expansion of the Antarctic ice sheet. *Paleoceanography*, *28*, 42–53. https://doi.org/10.1002/palo.20015

Beckage, B., & Ellingwood, C. (2008). Fire feedbacks with vegetation and alternative stable states. *Complex Systems*, *18*, 159–173. https://doi.org/10.25088/ComplexSystems.18.1.159

Bolton, C. T., Hernández-Sánchez, M. T., Fuertes, M.-Á., González-Lemos, S., Abrevaya, L., Mendez-Vicente, A., et al. (2016). Decrease in coccolithophore calcification and CO_2 since the middle Miocene. *Nature Communications*, *7*, 10,284. https://doi.org/10.1038/ncomms10284

Bourget, J., Zaragosi, S., Rodriguez, M., Fournier, M., Garlan, T., & Chamot-Rooke, N. (2013). Late Quaternary megaturbidites of the Indus fan: Origin and stratigraphic significance. *Marine Geology*, *336*, 10–23. https://doi.org/10.1016/j.margeo.2012.11.011

Brown, C. (2008). *Palynological techniques*. AASP Special Publications. Q5

Calvès, G., Huuse, M., Clift, P. D., & Brusset, S. (2015). Giant fossil mass wasting off the coast of West India: The Nataraja submarine slide. *Earth and Planetary Science Letters*, *432*, 265–272. https://doi.org/10.1016/j.epsl.2015.10.022

Caner, L., Seen, D. L., Gunnell, Y., Ramesh, B. R., & Bourgeon, G. (2007). Spatial heterogeneity of land cover response to climatic change in the Nilgiri highlands (southern India) since the last glacial maximum. *The Holocene*, *17*, 195–205. https://doi.org/10.1177/0959683607075833

Cerling, T. E., Harris, J. M., MacFadden, B. J., Leakey, M. G., Quade, J., Eisenmann, V., & Ehleringer, J. R. (1997). Global vegetation change through the Miocene/Pliocene boundary. *Nature*, *389*, 153–158.

Clift, P., Giosan, L., & Carter, A. (2010). Monsoon control over erosion patterns in the Western Himalaya: Possible feed-backs into the tectonic evolution. Monsoon evolution and tectonic-climate linkage in Asia. *Special Publication*, *342*, 181–213.

Clift, P. D., Zhou, P., Stockli, D. F., & Blusztajn, J. (2019). Regional Pliocene exhumation of the lesser Himalaya in the Indus drainage. *Solid Earth*, *10*, 647–661. https://doi.org/10.5194/se-10-647-2019

Contreras-Rosales, L. A., Jennerjahn, T., Tharammal, T., Meyer, V., Lückge, A., Paul, A., & Schefuß, E. (2014). Evolution of the Indian summer monsoon and terrestrial vegetation in the Bengal region during the past 18 ka. *Quaternary Science Reviews*, *102*, 133–148. https://doi.org/10.1016/j.quascirev.2014.08.010

Cotton, J. M., Cerling, T. E., Hoppe, K. A., Mosier, T. M., & Still, C. J. (2016). Climate, CO_2, and the history of North American grasses since the Last Glacial Maximum. *Science Advances*, *2*(3). https://doi.org/10.1126/sciadv.1501346

Dahl, K. A., Oppo, D. W., Eglinton, T. I., Hughen, K. A., Curry, W. B., & Sirocko, F. (2005). Terrigenous plant wax inputs to the Arabian Sea: Implications for the reconstruction of winds associated with the Indian monsoon. *Geochimica et Cosmochimica Acta*, *69*, 2547–2558. https://doi.org/10.1016/j.gca.2005.01.001

Dantas, V. D. L., Hirota, M., Oliveira, R. S., & Pausas, J. G. (2016). Disturbance maintains alternative biome states. *Ecology Letters*, *19*, 12–19. https://doi.org/10.1111/ele.12537

Das, A., Nagendra, H., Anand, M., & Bunyan, M. (2015). Topographic and bioclimatic determinants of the occurrence of forest and grassland in tropical montane forest-grassland mosaics of the Western Ghats, India. *PLoS ONE*, *10*(6), e0130566. https://doi.org/10.1371/journal.pone.0130566

Derry, L. A., & France-Lanord, C. (1996). Neogene growth of the sedimentary organic carbon reservoir. *Paleoceanography*, *11*, 267–275.

Ehleringer, J. R., Cerling, T. E., & Helliker, B. R. (1997). C-4 photosynthesis, atmospheric CO_2 and climate. *Oecologia*, *112*(3), 285–299. https://doi.org/10.1007/s004420050311

Feakins, S., de Menocal, P., & Eglinton, T. (2005). Biomarker records of late Neogene changes in East African vegetation. *Geology*, *33*, 977–980.

Feakins, S., Levin, N., Liddy, H., Sieracki, A., Eglinton, T., & Bonnefille, R. (2013). Northeast African vegetation change over 12 million years. *Geology*, *41*, 295–298. https://doi.org/10.1130/G33845.1

Feakins, S., & Sessions, A. L. (2010). Controls on the D/H ratios of plant leaf waxes from an arid ecosystem. *Geochimica et Cosmochimica Acta*, *74*, 2128–2141. https://doi.org/10.1016/j.gca.2010.01.016

Feakins, S. J. (2013). Pollen-corrected leaf wax D/H reconstructions of northeast African hydrological changes during the late Miocene. *Palaeogeography, Palaeoclimatology, Palaeoecology*, *374*, 62–71. https://doi.org/10.1016/j.palaeo.2013.01.004

Feakins, S. J. (2020). Indus fan, plant biomarkers and microfossils, 10–5 million years, In supplement to:. In S. J. Feakins, H. M. Liddy, L. Tauxe, V. Galy, X. Feng, J. E. Tierney, Y. Miao, & S. Warny (Eds.), *Late Miocene C_4 expansion and hydrological change in the Indus River catchment, paleoceanography and paleoclimatology*. NOAA. https://www.ncdc.noaa.gov/paleo/study/28792 Q6 Q7

Feakins, S. J., Bentley, L. P., Salinas, N., Shenkin, A., Blonder, B., Goldsmith, G. R., et al. (2016). Plant leaf wax biomarkers capture gradients in hydrogen isotopes of precipitation from the Andes and Amazon. *Geochimica et Cosmochimica Acta*, *182*, 155–172. https://doi.org/10.1016/j.gca.2016.03.018

Feakins, S. J., Kirby, M. E., Cheetham, M. I., Ibarra, Y., & Zimmerman, S. R. H. (2014). Fluctuation in leaf wax D/H ratio from a southern California lake records significant variability in isotopes in precipitation during the late Holocene. *Organic Geochemistry*, *66*, 48–59. https://doi.org/10.1016/j.orggeochem.2013.10.015

Feakins, S. J., Wu, M. S., Ponton, C., Galy, V., & West, A. J. (2018). Dual isotope evidence for sedimentary integration of plant wax biomarkers across an Andes-Amazon elevation transect. *Geochimica et Cosmochimica Acta*, *242*, 64–81. https://doi.org/10.1016/j.gca.2018.09.007

France-Lanord, C., & Derry, L. A. (1997). Organic carbon burial forcing of the carbon cycle from Himalayan erosion. *Nature*, *390*, 65–67.

Freeman, K. H., & Colarusso, L. A. (2001). Molecular and isotopic records of C4 grassland expansion in the late Miocene. *Geochimica et Cosmochimica Acta*, *65*, 1439–1454.

Galy, V., Eglinton, T., France-Lanord, C., & Sylva, S. (2011). The provenance of vegetation and environmental signatures encoded in vascular plant biomarkers carried by the Ganges-Brahmaputra rivers. *Earth and Planetary Science Letters*, *304*, 1–12. https://doi.org/10.1016/j.epsl.2011.02.003

Garcin, Y., Schefuß, E., Schwab, V. F., Garreta, V., Gleixner, G., Vincens, A., et al. (2014). Reconstructing C_3 and $_{C4}$ vegetation cover using *n*-alkane carbon isotope ratios in recent lake sediments from Cameroon, Western Central Africa. *Geochimica et Cosmochimica Acta*, *142*, 482–500. https://doi.org/10.1016/j.gca.2014.07.004

Ghosh, S., Sanyal, P., & Kumar, R. (2017). Evolution of C_4 plants and controlling factors: Insight from *n*-alkane isotopic values of NW Indian Siwalik paleosols. *Organic Geochemistry*, *110*, 110–121. https://doi.org/10.1016/j.orggeochem.2017.04.009

Gradstein, F. M., Ogg, J. G., Schmitz, M. D., & Ogg, G. M. (2012). *The geologic time scale 2012*. Boston: Elsevier.

Guan, K., Wood, E. F., Medvigy, D., Kimball, J., Pan, M., Caylor, K. K., et al. (2014). Terrestrial hydrological controls on land surface phenology of African savannas and woodlands. *Journal of Geophysical Research: Biogeosciences*, *119*, 1652–1669. https://doi.org/10.1002/2013jg002572

Gupta, A. K., Yuvaraja, A., Prakasam, M., Clemens, S. C., & Velu, A. (2015). Evolution of the South Asian monsoon wind system since the late Middle Miocene. *Palaeogeography, Palaeoclimatology, Palaeoecology*, *438*, 160–167. https://doi.org/10.1016/j.palaeo.2015.08.006

Hein, C. J., Galy, V., Galy, A., France-Lanord, C., Kudrass, H., & Schwenk, T. (2017). Post-glacial climate forcing of surface processes in the Ganges–Brahmaputra river basin and implications for carbon sequestration. *Earth and Planetary Science Letters*, *478*, 89–101. https://doi.org/10.1016/j.epsl.2017.08.013

Hemingway, J. D., Schefuß, E., Dinga, B. J., Pryer, H., & Galy, V. V. (2016). Multiple plant-wax compounds record differential sources and ecosystem structure in large river catchments. *Geochimica et Cosmochimica Acta*, *184*, 20–40. https://doi.org/10.1016/j.gca.2016.04.003

Herbert, T. D., Lawrence, K. T., Tzanova, A., Peterson, L. C., Caballero-Gill, R., & Kelly, C. S. (2016). Late Miocene global cooling and the rise of modern ecosystems. *Nature Geoscience*, *9*, 843. https://doi.org/10.1038/ngeo2813

Higgins, S. I., & Scheiter, S. (2012). Atmospheric CO_2 forces abrupt vegetation shifts locally, but not globally. *Nature*, *488*(7410), 209–212. https://doi.org/10.1038/nature11238

Hoetzel, S., Dupont, L., Schefusz, E., Rommerskirchen, F., & Wefer, G. (2013). The role of fire in Miocene to Pliocene C_4 grassland and ecosystem evolution. *Nature Geosci*, *6*, 1027–1030. https://doi.org/10.1038/ngeo1984

Holbourn, A., Kuhnt, W., Clemens, S., Prell, W., & Andersen, N. (2013). Middle to late Miocene stepwise climate cooling: Evidence from a high-resolution deep-water isotope curve spanning 8 million years. *Paleoceanography*, *28*, 688–699. https://doi.org/10.1002/2013pa002538

Holbourn, A. E., Kuhnt, W., Clemens, S. C., Kochhann, K. G. D., Jöhnck, J., Lübbers, J., & Andersen, N. (2018). Late Miocene climate cooling and intensification of southeast Asian winter monsoon. *Nature Communications*, *9*(1), 1584. https://doi.org/10.1038/s41467-018-03950-1

Hopmans, E. C., Weijers, J. W. H., Schefuß, E., Herfort, L., Sinninghe Damsté, J. S., & Schouten, S. (2004). A novel proxy for terrestrial organic matter in sediments based on branched and isoprenoid tetraether lipids. *Earth and Planetary Science Letters*, *224*, 107–116. https://doi.org/10.1016/j.epsl.2004.05.012

Huang, Y., Clemens, S. C., Liu, W., Wang, Y., & Prell, W. L. (2007). Large-scale hydrological change drove the late Miocene C_4 plant expansion in the Himalayan foreland and Arabian peninsula. *Geology*, *35*, 531–534. https://doi.org/10.1130/G23666A

IAEA/WMO (2019) Global network of isotopes in precipitation. The GNIP Database. Accessible at: http://www.iaea.org/water.

Ivory, S. J., & Lezine, A. M. (2009). Climate and environmental change at the end of the Holocene Humid Period: A pollen record off Pakistan. *Comptes Rendus Geoscience*, *341*, 760–769. https://doi.org/10.1016/j.crte.2008.12.009

Karp, A. T., Behrensmeyer, A. K., & Freeman, K. H. (2018). Grassland fire ecology has roots in the late Miocene. *Proceedings of the National Academy of Sciences*, *115*, 12,130–12,135. https://doi.org/10.1073/pnas.1809758115

Keigwin, L. D. (1979). Late Cenozoic stable isotope stratigraphy and paleoceanography of DSDP sites from the east equatorial and central north Pacific Ocean. *Earth and Planetary Science Letters*, *45*, 361–382. https://doi.org/10.1016/0012-821X(79)90137-7

Kessarkar, P. M., Rao, V. P., Ahmad, S. M., & Babu, G. A. (2003). Clay minerals and Sr–Nd isotopes of the sediments along the western margin of India and their implication for sediment provenance. *Marine Geology*, *202*, 55–69. https://doi.org/10.1016/S0025-3227(03)00240-8

Kroon, D. (1988). Distribution of extant planktic foraminiferal assemblages in Red Sea and northern Indian Ocean surface waters. In D. Kroon (Ed.), *Planktonic foramingers as tracers of ocean-climate history*, (p. 346). Amsterdam: Free Univ. Press. Q8

Kroon, D., Steens, T. and Troelstra, S.R. (1991) Onset of monsoonal related upwelling in the western Arabian Sea as revealed by planktonic foraminifers. Proc., scientific results, ODP, leg 117, Oman margin/Neogene package, 257-263.

Kusch, S., Rethemeyer, J., Schefuß, E., & Mollenhauer, G. (2010). Controls on the age of vascular plant biomarkers in Black Sea sediments. *Geochimica Et Cosmochimica Acta*, *74*, 7031–7047. https://doi.org/10.1016/j.gca.2010.09.005

Lear, C., Elderfield, H., & Wilson, P. (2000). Cenozoic deep-sea temperatures and global ice volumes from Mg/Ca in benthic foraminiferal calcite. *Science*, *287*(5451), 269–272. https://doi.org/10.1126/science.287.5451.269

Lear, C. H., Coxall, H. K., Foster, G. L., Lunt, D. J., Mawbey, E. M., Rosenthal, Y., et al. (2015). Neogene ice volume and ocean temperatures: Insights from infaunal foraminiferal Mg/Ca paleothermometry. *Paleoceanography*, *30*, 1437–1454. https://doi.org/10.1002/2015pa002833

Lee, J.-E. (2019). Understanding neogene oxygen isotopes in the Southern Great Plains using isotope-enabled general circulation model simulations. *Journal of Geophysical Research: Atmospheres*, *124*, 2452–2464. https://doi.org/10.1029/2018jd028894

Levin, N. E. (2015). Environment and climate of early human evolution. *Annual Review of Earth and Planetary Sciences*, *43*, 405–429. https://doi.org/10.1146/annurev-earth-060614-105310

Liddy, H. M., Feakins, S. J., & Tierney, J. E. (2016). Cooling and drying in northeast Africa across the Pliocene. *Earth and Planetary Science Letters*, *449*, 430–438. https://doi.org/10.1016/j.epsl.2016.05.005

Locarnini, A.R., Mishonov, A., Antonov, I.J., Boyer, P.T., Garcia, H., Baranova, K.O., et al. (2010) World ocean atlas 2009, vol. 1: Temperature, p. 184.

Lutsko, N. J., Marshall, J., & Green, B. (2019). Modulation of monsoon circulations by cross-equatorial ocean heat transport. *Journal of Climate*, *32*, 3471–3485. https://doi.org/10.1175/jcli-d-18-0623.1

Makou, M., Eglinton, T., McIntyre, C., Montluçon, D., Antheaume, I., & Grossi, V. (2018). Plant wax *n*-alkane and *n*-alkanoic acid signatures overprinted by microbial contributions and old carbon in meromictic lake sediments. *Geophysical Research Letters*, *45*, 1049–1057. https://doi.org/10.1002/2017GL076211

Marret, F., & Zonneveld, K. A. F. (2003). Atlas of modern organic-walled dinoflagellate cyst distribution. *Review of Palaeobotany and Palynology*, *125*, 1–200. https://doi.org/10.1016/S0034-6667(02)00229-4

Mejía, L. M., Méndez-Vicente, A., Abrevaya, L., Lawrence, K. T., Ladlow, C., Bolton, C., et al. (2017). A diatom record of CO_2 decline since the late Miocene. *Earth and Planetary Science Letters*, *479*, 18–33. https://doi.org/10.1016/j.epsl.2017.08.034

Métivier, F., Gaudemer, Y., Tapponnier, P., & Klein, M. (1999). Mass accumulation rates in Asia during the Cenozoic. *Geophysical Journal International*, *137*, 280–318. https://doi.org/10.1046/j.1365-246X.1999.00802.x

Miao, Y., Wu, F., Warny, S., Fang, X., Lu, H., Fu, B., et al. (2019). Miocene fire intensification linked to continuous aridification on the Tibetan Plateau. *Geology*, *47*, 303–307. https://doi.org/10.1130/g45720.1

Milliman, J. D., & Syvitski, J. P. M. (1992). Geomorphic/tectonic control of sediment discharge to the ocean: The importance of small mountainous rivers. *The Journal of Geology*, *100*, 525–544.10.1086/629606.

Murakami, H., Vecchi, G. A., & Underwood, S. (2017). Increasing frequency of extremely severe cyclonic storms over the Arabian Sea. *Nature Climate Change*, *7*(12), 885–889. https://doi.org/10.1038/s41558-017-0008-6

Osborne, C. P. (2008). Atmosphere, ecology and evolution: What drove the Miocene expansion of C-4 grasslands? *Journal of Ecology*, *96*(1), 35–45. https://doi.org/10.1111/j.1365-2745.2007.01323.x

Pagani, M., Freeman, K. H., & Arthur, M. A. (1999). Late Miocene atmospheric CO_2 concentrations and the expansion of C-4 grasses. *Science*, *285*, 876–879.

Pandey, D., Clift, P., Kulhanek, D., Andò, S., Bendle, J., Bratenkov, S., et al. (2015). Expedition 355 preliminary report: Arabian Sea monsoon. *Proceedings of the International Ocean Discovery Program*, *2015*, 1–46.

Polissar, P. J., Rose, C., Uno, K. T., Phelps, S. R., & deMenocal, P. (2019). Synchronous rise of African C4 ecosystems 10 million years ago in the absence of aridification. *Nature Geoscience*, *12*, 657–660. https://doi.org/10.1038/s41561-019-0399-22

Prins, M. A., Postma, G., & Weltje, G. J. (2000). Controls on terrigenous sediment supply to the Arabian Sea during the late Quaternary: The Makran continental slope. *Marine Geology*, *169*, 351–371. https://doi.org/10.1016/S0025-3227(00)00087-6

Quade, J., & Cerling, T. E. (1995). Expansion of C-4 grasses in the Late Miocene of Northern Pakistan—Evidence from stable isotopes in paleosols. *Palaeogeography Palaeoclimatology Palaeoecology*, *115*, 91–116.

Quade, J., Cerling, T. E., & Bowman, J. R. (1989). Development of Asian monsoon revealed by marked ecological shift during the latest Miocene in Northern Pakistan. *Nature*, *342*, 163–166.

Rodriguez, M., Chamot-Rooke, N., Huchon, P., Fournier, M., & Delescluse, M. (2014). The Owen Ridge uplift in the Arabian Sea: Implications for the sedimentary record of Indian monsoon in Late Miocene. *Earth and Planetary Science Letters*, *394*, 1–12.

Routledge, C. M., Kulhanek, D. K., Tauxe, L., Scardia, G., Singh, A. D., Steinke, S., et al. (2019). A revised chronostratigraphic framework for International Ocean Discovery Program Expedition 355 sites in Laxmi Basin, eastern Arabian Sea. *Geological Magazine*, 1–18. https://doi.org/10.1017/S0016756819000104

Sachse, D., Billault, I., Bowen, G. J., Chikaraishi, Y., Dawson, T. E., Feakins, S. J., et al. (2012). Molecular paleohydrology: Interpreting the hydrogen-isotopic composition of lipid biomarkers from photosynthesizing organisms. *Annual Review of Earth and Planetary Sciences*, *40*, 221–249. https://doi.org/10.1146/annurev-earth-042711-105535

Schouten, S., Huguet, C., Hopmans, E. C., Kienhuis, M. V. M., & Damste, J. S. S. (2007). Analytical methodology for TEX86 paleothermometry by high-performance liquid chromatography/atmospheric pressure chemical ionization-mass spectrometry. *Analytical Chemistry*, *79*(7), 2940–2944. https://doi.org/10.1021/ac062339v

Schouten, S., van der Meer, M. T. J., Hopmans, E. C., Rijpstra, W. I. C., Reysenbach, A. L., Ward, D. M., & Damste, J. S. S. (2007). Archaeal and bacterial glycerol dialkyl glycerol tetraether lipids in hot springs of Yellowstone National Park. *Applied and Environmental Microbiology*, *73*(19), 6181–6191. https://doi.org/10.1128/AEM.00630-07

Smith, F., & Freeman, K. (2006). Influence of physiology and climate on dD of leaf wax *n*-alkanes from C_3 and C_4 grasses. *Geochimica et Cosmochimica Acta*, *70*, 1172–1187.

Sosdian, S. M., Greenop, R., Hain, M. P., Foster, G. L., Pearson, P. N., & Lear, C. H. (2018). Constraining the evolution of neogene ocean carbonate chemistry using the boron isotope pH proxy. *Earth and Planetary Science Letters*, *498*, 362–376. https://doi.org/10.1016/j.epsl.2018.06.017

Staver, A. C., Archibald, S., & Levin, S. A. (2011). The global extent and determinants of savanna and forest as alternative biome states. *Science*, *334*(6053), 230–232. https://doi.org/10.1126/science.1210465

Suh, Y. J., Diefendorf, A. F., Bowen, G. J., Cotton, J. M., & Ju, S.-J. (2019). Plant wax integration and transport from the Mississippi River basin to the Gulf of Mexico inferred from GIS-enabled isoscapes and mixing models. *Geochimica et Cosmochimica Acta*, *257*, 131–149. https://doi.org/10.1016/j.gca.2019.04.022

Tauxe, L. and Feakins, S.J. (n.d.) A re-assessment of the timing of the late Miocene C_3-C_4 transition. Paleoceanography and Paleoclimatology manuscript: 2020PA003857.

Tierney, J. E., Pausata, F. S. R., & deMenocal, P. (2016). Deglacial Indian monsoon failure and North Atlantic stadials linked by Indian Ocean surface cooling. *Nature Geoscience*, *9*(1), 46–50. https://doi.org/10.1038/ngeo2603, http://www.nature.com/ngeo/journal/v9/n1/abs/ngeo2603.html#supplementary-information

Tierney, J. E., & Tingley, M. P. (2014). A Bayesian, spatially-varying calibration model for the TEX86 proxy. *Geochimica et Cosmochimica Acta*, *127*, 83–106. https://doi.org/10.1016/j.gca.2013.11.026

Uno, K. T., Cerling, T. E., Harris, J. M., Kunimatsu, Y., Leakey, M. G., Nakatsukasa, M., & Nakaya, H. (2011). Late Miocene to Pliocene carbon isotope record of differential diet change among East African herbivores. *Proceedings of the National Academy of Sciences of the United States of America*, *108*(16), 6509–6514. https://doi.org/10.1073/pnas.1018435108

Uno, K. T., Polissar, P. J., Jackson, K. E., & deMenocal, P. B. (2016). Neogene biomarker record of vegetation change in eastern Africa. *Proceedings of the National Academy of Sciences*, *113*(23), 6355–6363. https://doi.org/10.1073/pnas.1521267113

Vögeli, N., Najman, Y., van der Beek, P., Huyghe, P., Wynn, P. M., Govin, G., et al. (2017). Lateral variations in vegetation in the Himalaya since the Miocene and implications for climate evolution. *Earth and Planetary Science Letters*, *471*, 1–9. https://doi.org/10.1016/j.epsl.2017.04.037

Whiteside, J. H., Olsen, P. E., Eglinton, T. I., Cornet, B., McDonald, N. G., & Huber, P. (2011). Pangean great lake paleoecology on the cusp of the end-Triassic extinction. *Palaeogeography, Palaeoclimatology, Palaeoecology*, *301*, 1–17. https://doi.org/10.1016/j.palaeo.2010.11.025

Yu, Z., Colin, C., Wan, S., Saraswat, R., Song, L., Xu, Z., et al. (2019). Sea level-controlled sediment transport to the eastern Arabian Sea over the past 600 kyr: Clay minerals and SrNd isotopic evidence from IODP site U1457. *Quaternary Science Reviews*, *205*, 22–34. https://doi.org/10.1016/j.quascirev.2018.12.006

Zhang, Y. G., Pearson, A., Benthien, A., Dong, L., Huybers, P., Liu, X., & Pagani, M. (2019). Refining the alkenone-pCO_2 method I: Lessons from the Quaternary glacial cycles. *Geochimica et Cosmochimica Acta*, *260*, 177–191. https://doi.org/10.1016/j.gca.2019.06.032